Materials Science & Engineering A xxx (xxxx) xxx

Contents lists available at ScienceDirect

Materials Science & Engineering A

journal homepage: http://www.elsevier.com/locate/msea

A full-field crystal plasticity model including the effects of precipitates: Application to monotonic, load reversal, and low-cycle fatigue behavior of Inconel 718

Adnan Eghtesad, Marko Knezevic *

Department of Mechanical Engineering, University of New Hampshire, Durham, NH, 03824, USA

ARTICLE INFO

Keywords:
Microstructures
Fatigue
Crystal plasticity
Cyclic loading
Inconel 718

ABSTRACT

This work advances a recently developed high-performance, full-field elasto-viscoplastic fast Fourier transform (MPI-ACC-EVPCUFFT) formulation to model large plastic deformation and low-cycle fatigue behavior of Inconel 718 (IN718). Specifically, the recently developed model of Eghtesad et al., 2020 [1] incorporating a strain rate, temperature, and strain-path sensitive hardening law based on the evolution of dislocation density and a slip system-level back-stress law influencing the resolved shear stress is advanced in several aspects. First, strengthening effects due to grain size and shape, solid solution, shearing of small precipitates, and Orowan looping around larger precipitates are incorporated into the initial slip resistance, which evolves with the hardening law including the latent hardening. Second, the resolved shear stress on the slip plane in the direction of slip is altered by accounting for the two orthogonal shear stress components and the three normal stress components, in addition to the slip system-level kinematic effects. The model is used to interpret the complex mechanical behavior and microstructural data for samples of alloy IN718 in additively manufactured (AM) forms before and after hot isostatic pressing (HIP) and in a wrought form. Voxel-based microstructural cells consistent with the characterization data are synthetically constructed to initialize the model setups for predicting simple compression, tension, load reversal, and low cycle fatigue behavior of the alloy. Variation in the microstructural features such as the distribution of grain size and shape, crystallographic texture, content of annealing twins, and precipitates among the samples facilitated reliable calibration and validation of the model parameters. Predicted anisotropy, tension/compression asymmetry, non-linear unloading upon the load reversal, the Bauschinger effect, reverse hardening, texture evolution as well as cyclic hardening/softening along with the mean stress relaxation during low-cycle fatigue are in good agreement with the corresponding experimental data for the alloy. Furthermore, the simulations based on the high-resolution microstructural cells facilitated the discussion of the mechanical fields induced by microstructure, and especially annealing twins.

1. Introduction

Alloy Inconel 718 (IN718) is a Ni-based superalloy known for a range of desired properties such as high toughness, strength, creep, and corrosion resistance [2–8]. The processing of the alloy components such as turbine parts like disks, blades, rings, and casings involves casting, forging, rolling, forming, machining, and heat treating. Microstructure of the alloy continuously evolves during the thermo-mechanical processing governing its structural properties. As parts are often of complicated shape, cost of machining of such parts is relatively high because the cutting tools wear rapidly. Parts of the alloy can also be printed using additive manufacturing (AM) technologies from powders substantially reducing the cost of machining [9–12]. For understanding the evolution of structure-property relationships of the alloy, it is essential to understand the underlying micro-scale deformation mechanisms leading to microstructure evolution. Such links can be established using polycrystal plasticity modeling, which can facilitate evaluating the in-service behavior as well as designing the processing paths for optimal properties for the alloy. The in-service loading is often cyclic. Thus, fatigue fracture is the most critical design condition. However, the development of polycrystal plasticity models for the alloy is challenging because the material can exhibit complex grain structure

* Corresponding author. Department of Mechanical Engineering, University of New Hampshire, 33 Academic Way, Kingsbury Hall, W119, Durham, NH, 03824, USA.
E-mail address: marko.knezevic@unh.edu (M. Knezevic).

https://doi.org/10.1016/j.msea.2020.140478
Received 6 September 2020; Received in revised form 25 October 2020; Accepted 27 October 2020
Available online 3 November 2020
0921-5093/© 2020 Elsevier B.V. All rights reserved.

including annealing twins and several kinds of precipitates interacting with dislocations governing its anisotropic hardening. In particular, the development of models for capturing the mechanisms of the cyclic deformation is challenging.

The properties of the alloy are primarily governed by the γ' and γ'' intermetallic second phases. Additionally, δ and Laves phases can be present in the microstructure of the alloy. However, presence of these phases is usually minimized by heat treatments [13,14]. Laves phases are detrimental to mechanical properties, while δ precipitates can also be detrimental to properties unless they form at the grain boundaries, where they improve the material's creep behavior by preventing grain boundary sliding as a creep mechanism [15,16]. Finally, some MC carbides can be present in the microstructure. The γ' phase is a Ni_3(Ti, Al) compound of a spherical shape [3,17] with face-centered cubic (FCC) crystal structure [18]. Size of coherent γ' is in the range 10 nm–50 nm [18]. The γ'' phase is a Ni_3Nb compound of a disk shape with body-centered tetragonal (BCT) structure [3,18]. Its size is similar to the size of the γ' shearable phase. The δ phase is also Ni_3Nb but needle-shaped with typical length about 1–8 μm [15,19,20]. Since coarser, these precipitates are incoherent with the γ matrix and dislocations loop around them. As volume fraction and distribution of these phases depend on processing, creating the alloy by AM can result with globular δ phase of variable size [21–23]. The shearable fractions of γ', γ'', and δ phases due to their small size and coherency with γ, leaves an anti-phase boundary (APB) contributing to some additional strengthening of the overall alloy [24–26]. The values for APB energies for these shearable phases have been presented in our earlier studies [27,28]. While some cubic slip $\{001\}\langle 110\rangle$ has been observed at wrought processing temperatures [29–32], the octahedral slip systems $\{111\}\langle 1\bar{1}0\rangle$ carry out the plastic deformation of γ matrix at room temperature.

The mechanical response of the alloy is anisotropic showing also some tension-compression (T-C) asymmetry [33–35]. Such behavior of the alloy originates from its complex microstructural features and crystallographic slip being influenced not only by the resolved shear stress on the slip plane in the direction of slip is but also by the two orthogonal shear stress components and the three normal stress components as well as by the slip system kinematic effects [36–40]. Furthermore, the alloy exhibits cyclic hardening and then prolonged cyclic softening during low-cycle fatigue (LCF) [10]. Microstructure-based models have been used to study relationships between microstructure, deformation mechanisms, and local and overall response of the alloy [2,35,41]. The focus was primarily on quasi-static monotonic behavior, while less attention was dedicated to modeling of fatigue behavior of the alloy.

Microstructure evolution during LCF in alloy IN718 and several other similar alloys has been studied experimentally in a number of works [17,42–45]. In particular, the observation of the short period of cyclic hardening followed by a prolonged period of cyclic softening as a function of strain amplitudes was investigated. The cycle at which transition from hardening to softening occurs was found to depend on strain amplitude of the fatigue hysteresis loops. The observations by transmission electron microscopy (TEM) revealed that both γ' and γ'' precipitates are sheared during the cyclic deformation, while planar deformation bands form on the octahedral slip planes. The comparison of the initial and cyclically deformed microstructures showed that the sizes of the precipitates have substantially reduced. The reduction in size is rationalized as the primary reason for the softening during the cyclic loading [42]. The precipitates are sheared by $a/2\langle 110\rangle$ dislocation pairs, where the leading dislocations disorders the structure creating an APB followed by the trailing dislocations restoring the order with no evidence of stacking fault mode of deformation [46,47]. After the cutting for the first time, the dislocations would successively shear the precipitates again and again as the cyclic deformation continues reducing the size of the particles to an extent that the particles would offer very little or no resistance to the glide of dislocations [48]. The stress required to shear the smaller and smaller particles is continuously reducing. Moreover, the preferential gliding paths in $\{111\}$ deformation bands with decreasing resistance to glide is being established during the progressive deformation. The formation of planar slip bands while shearing of coherent and ordered precipitates by pairs of dislocations moving on the octahedral slip planes is facilitated because of no cross-slip occurring during cyclic deformation in the alloy. The bands arranged in arrays restricting the dislocation movement are the secondary reason for the observed cyclic softening [49]. The observed shearing of the precipitates occurred only during cyclic deformation, i.e. no shearing was observed during any monotonic deformation. These bands become essentially precipitate-free at the later stage of LCF [50]. Additionally, the softening in testing at elevated temperature can also be a consequence of time dependent coarsening of precipitates and resulting changes in their size and volume fraction [51].

While the cyclic behavior and the underlying micro-mechanisms have been well studied from the experimental viewpoint [45,52,53], the cyclic behavior of IN718 has been modeled primarily using phenomenological models without consideration of microstructural details [54,55]. These models combine non-linear isotropic and kinematic hardening to capture the main features of the cyclic deformation including the Bauchinger effect. However, they require a large number of fitting parameters not related to microstructure [56]. As a result, any change in the microstructure of IN718 requires time consuming and challenging experimental campaigns and refitting to determine a new set of parameters for the model. A significant improvement with respect to the phenomenological approaches can be obtained by involving microstructure-based models [41,57–59]. Here, the details of the elasto-plastic deformation are taken into account at the grain-level and the effective properties of a polycrystal are calculated using a homogenization scheme. The approach can take into account distributions of grain size and shape and texture on the mechanical response [60,61]. These models provide flexibility to predict material response as a function of microstructure with a relatively small number of fitting parameters in comparison with to macroscopic models but are significantly more computationally intensive. The present paper is a contribution involving a microstructure sensitive modeling.

The present work attempts to incorporate the phenomena pertaining to the deformation of IN718 into a full field crystal plasticity model of an elasto-visco-plastic fast Fourier transform (EVPFFT) type [62] to study monotonic, load reversal, and cyclic behavior recorded under strain control at different cyclic strain amplitudes of alloy IN718 as a function of the initial microstructure. The initial materials/microstructures used in the study were created via AM along with subsequent hot isostatic pressing (HIP) and finally wrought processing. Every material was heat treated (HT) after machining according to AMS 5663. We acknowledge that most of the experimental results have been presented in previous papers [10,21,23,27,28,63]. However, we include the relevant data to facilitate comparisons and for the sake of completeness of the present study. The recently developed MPI-ACC-EVPCUFFT model [1,64] incorporating a strain rate, temperature, and strain-path sensitive hardening law based on the evolution of forward and reverse dislocation density populations and an empirical slip system-level backstress law influencing the resolved shear stress is advanced. To this end, strengthening effects due to grain size and shape, solid solution, shearing of small precipitates, and Orowan looping around larger precipitates are incorporated into the initial slip resistance, which evolves with the hardening law including the latent hardening. Thus, the formation of APB in precipitates as mobile dislocations shear through them is included in the initial slip resistance. The Orowan looping enhances an intra-granular backstress, which is modeled using the law for intra-granular backstress. Second, the resolved shear stress on the slip plane in the direction of slip is adjusted by accounting for the two orthogonal shear stress components and the three normal stress components, in addition to the slip system kinematic effects. In order to reduce the computational cost for simulations and in particular

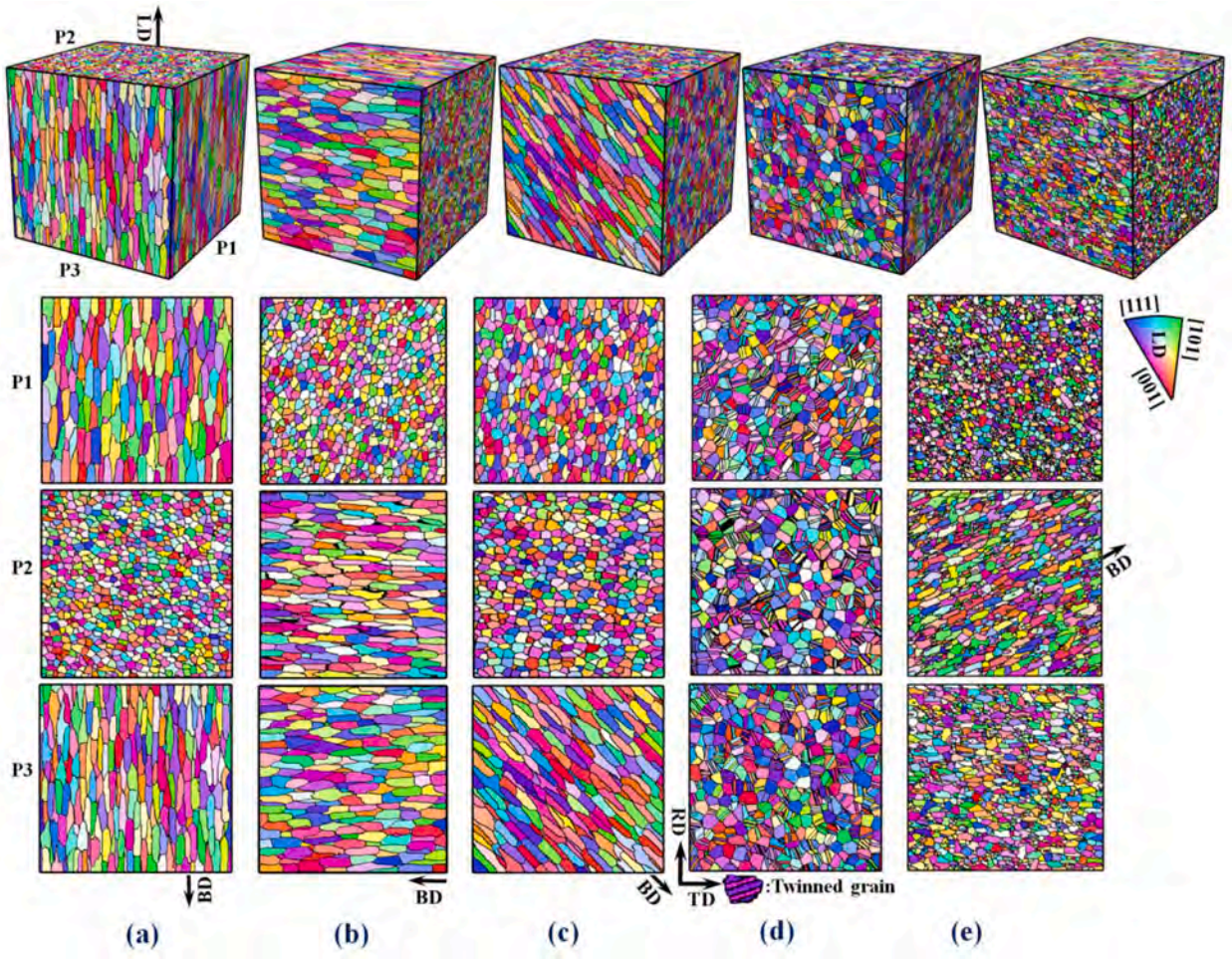

Fig. 1. Microstructural cells for simulations of IN718 Ni-based superalloy: (a) AM horizontal, (b) AM vertical, (c) AM diagonal, (d) wrought and (e) AM + HIP. The first row indicates the 3D RVE microstructures, while the second row shows the three perpendicular 2D projections. The build direction (BD) relative to the loading direction (LD) is indicated for the AM materials.

Table 1
Summary of microstructural cell parameters for DREAM3D. The parameters are based on the experimental data from Ref. [21].

	AM Vertical	AM Horizontal	AM Diagonal	AM + HIP	Wrought
# of grains	5963	5963	5963	75,921	16,122
RVE resolution	0.25^3	0.25^3	0.25^3	0.25^3	0.25^3
# of voxels	256^3	256^3	256^3	256^3	256^3
Average # of voxels per grain	2813	2813	2813	221.0	1041
Equivalent sphere diameter (ESD)	4.48–4.70	4.48–4.70	4.48–4.70	1.6–3.7	4.45–4.50
Feature aspect ratio (a/b, a/c)	5.2	5.2	5.2	3.5	1.0

simulating a large number of cycles, the MPI-ACC-EVPCUFFT code utilizes a Graphics Processing Units (GPU)-based hardware.

2. Modeling framework

The most commonly used crystal plasticity solvers capable of

Table 2
IN718 precipitate shearing/looping parameters [23,27,28].

Parameters	AM	AM + HIP	Wrought
$APB_{\gamma'}\ \left[\frac{mJ}{m^2}\right]$	207.0	207.0	207.0
$APB_{\gamma''}\ \left[\frac{mJ}{m^2}\right]$	378.0	378.0	378.0
$f_{\gamma'}$ [%]	6.5	5.4	6.5
$f_{\gamma''}$ [%]	8.4	17.7	17.8
f_{δ} [%]	5.9	1.1	1.3
f_{MC} [%]	1.9	0.5	0.9
$\mu_{\gamma'}$ [GPa]	78.2	78.2	78.2
$\mu_{\gamma''}$ [GPa]	72.6	72.6	72.6
μ_{δ} [GPa]	84.3	84.3	84.3
μ_{MC} [GPa]	182.0	182.0	182.0
$r_{\gamma'}$ [nm]	12.5	12.5	12.5
$r_{\gamma''}$ [nm]	4.2	4.2	4.2
r_{MC} [nm]	600.0	300.0	300.0
$r_{\delta,major}$ [nm]	1500.0	5000.0	10,000.0
$r_{\delta,minor}$ [nm]	300.0	200.0	700.0
r_{δ} [nm]	513.0	585.0	1698.0
$b_{\gamma'}$ [nm]	0.2549	0.2549	0.2549
$b_{\gamma''}$ [nm]	0.2563	0.2563	0.2563
b_{δ} [nm]	0.3217	0.3217	0.3217
b_{MC} [nm]	0.3153	0.3153	0.3153
$b_{IN718,\langle 110\rangle}$ [nm]	0.2492	0.2492	0.2492

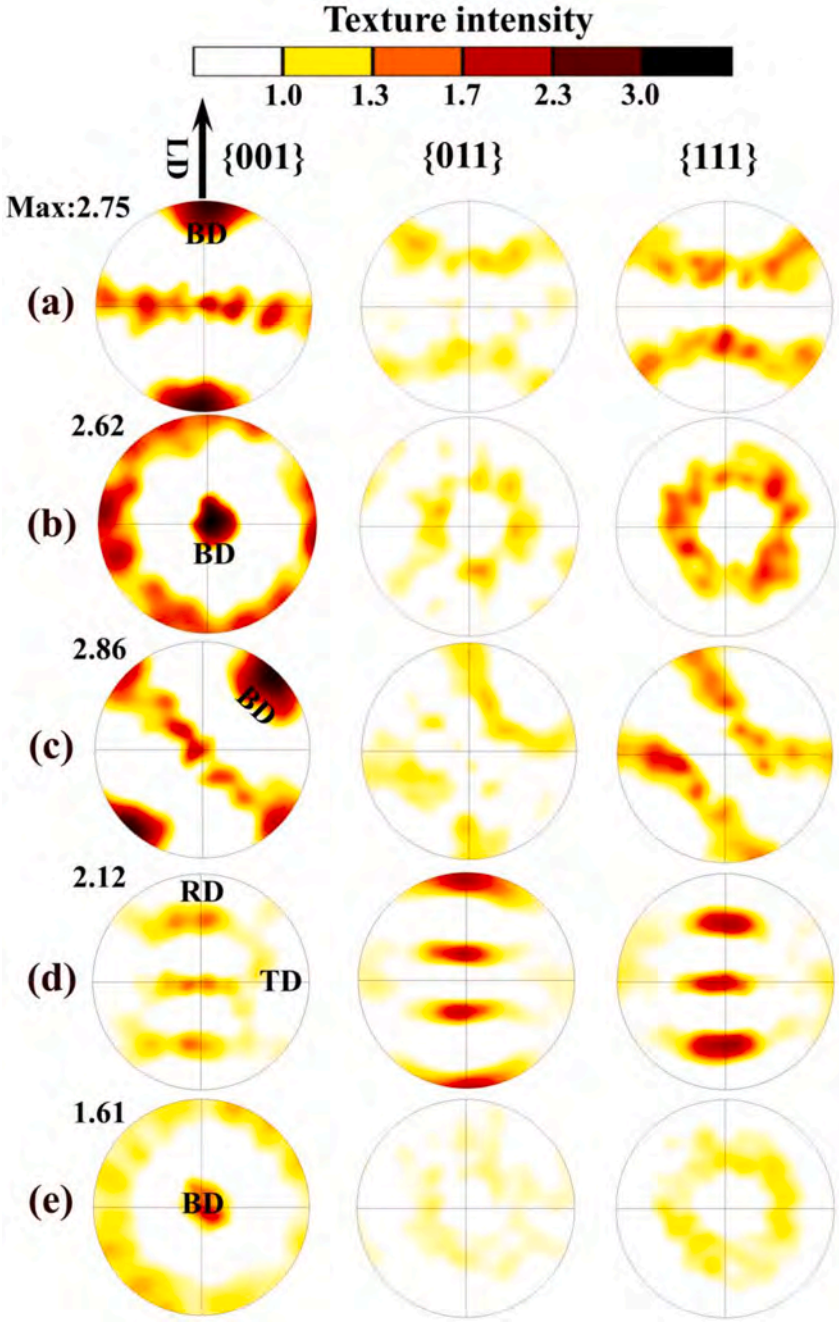

Fig. 2. Stereographic pole figures showing texture in: (a) AM vertical (b) AM horizontal (c) AM diagonal (d) wrought and (e) AM + HIP samples of the Ni-based IN718 superalloy relative to the loading direction (LD) [28]. The wrought material was a rolled shape forging with rolling direction (RD) and transverse direction (TD) indicated.

calculating spatial strain and stress fields over microstructural domains are the crystal plasticity finite element (CPFE) models [65–72], and Green's function-based EVPFFT models [62,73–75]. The FFT-based solvers are known to be computationally efficient [73]. Moreover, the accelerated versions of such codes running on distributed nodes of Central Processing Units (CPUs) [74] and GPU [1] have offered ultimate speed ups of multiples of hundreds allowing for simulations of high-resolution microstructures. In this work we use the Multi-GPU version of the code termed MPI-ACC-EVPCUFFT and further develop it for simulations of precipitate-hardened metallic super alloys such as IN718. In the notation we use, tensors are denoted by non-italic bold letters while scalars and tensor components are italic and not bold. For a contracted or dot product and uncontracted or tensor product, · and ⊗ symbols are used, respectively.

In the visco-plastic crystal plasticity formulation, plastic strain rate, $\dot{\boldsymbol{\varepsilon}}^p(\mathbf{x})$, shearing rate, $\dot{\gamma}^s$, and Cauchy stress, $\boldsymbol{\sigma}(\mathbf{x})$, are related at a single-crystal material point $\mathbf{x}$ using [76–79].

$$\dot{\boldsymbol{\varepsilon}}^p(\mathbf{x}) = \sum_{s=1}^{N} \mathbf{P}^s(\mathbf{x})\,\dot{\gamma}^s(\mathbf{x}) = \dot{\gamma}_0 \sum_{s=1}^{N} \mathbf{P}^s(\mathbf{x}) \left(\frac{\mathbf{P}^s(\mathbf{x}) \cdot \boldsymbol{\sigma}(\mathbf{x}) - \tau_{bs}^s(\mathbf{x})}{\tau_c^s(\mathbf{x})} \right)^n, \tag{1a}$$

$$\mathbf{P}_{ns}^s = c_1(\mathbf{t}^s \otimes \mathbf{b}^s) + c_2(\mathbf{t}^s \otimes \mathbf{n}^s) + c_3(\mathbf{n}^s \otimes \mathbf{n}^s) + c_4(\mathbf{t}^s \otimes \mathbf{t}^s) - (c_3 + c_4)(\mathbf{b}^s \otimes \mathbf{b}^s) \tag{1b}$$

$$\mathbf{P}_{sc}^s = \frac{1}{2}(\mathbf{b}^s \otimes \mathbf{n}^s + \mathbf{n}^s \otimes \mathbf{b}^s) \tag{1c}$$

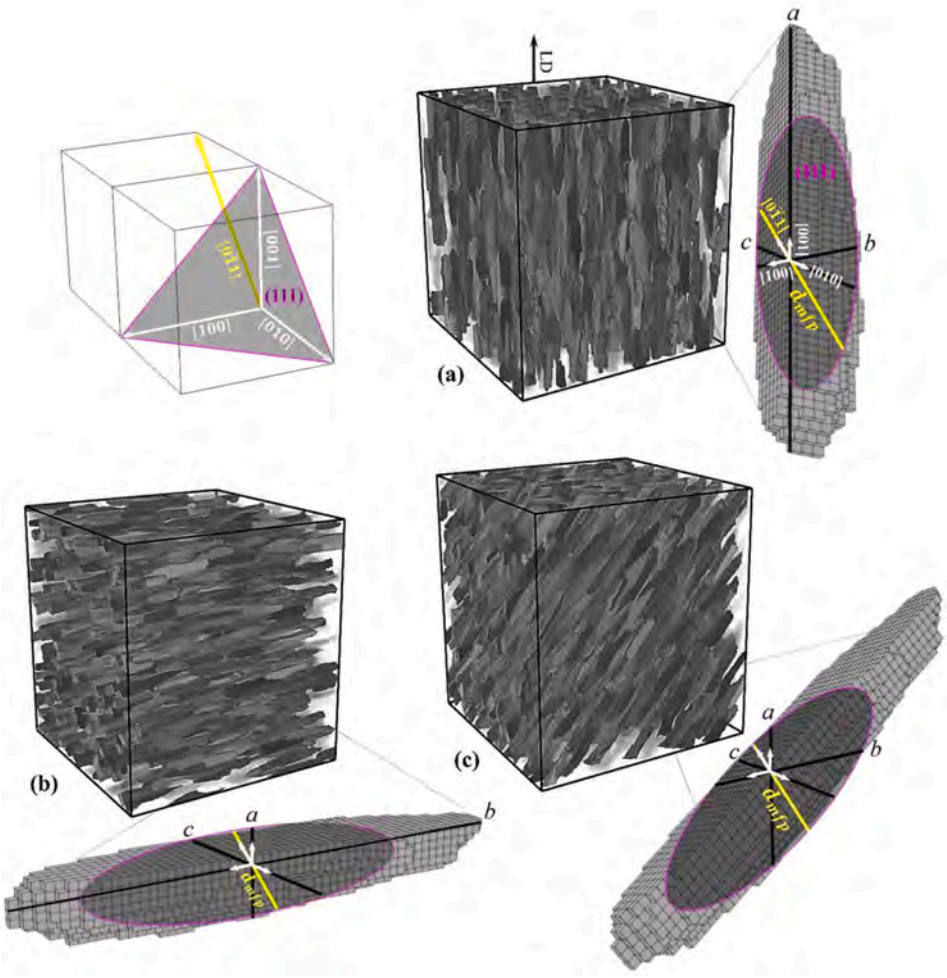

Fig. 3. Schematic depicting the effect of grain morphology on the mean-free-path, d_{mfp}^{s}, for a randomly selected crystal orientation with (111) glide plane in the [0$\bar{1}$1] direction. The grain shape is represented as an effective ellipsoid with its axes relative to the loading axis (LD) activating the same slip system in every ellipsoid: (a) AM vertical, (b) AM horizontal, and (c) AM diagonal microstructures.

Table 3
Effective grain shape per material [21].

	AM Vertical	AM Horizontal	AM Diagonal	AM + HIP	Wrought
a [μm]	130	25	75	280	105
b [μm]	25	130	75	80	105
c [μm]	25	25	25	80	105

Table 4
Single-crystal elastic constants for IN718 [27].

C_{11} [MPa]	242,200
C_{12} [MPa]	138,900
C_{44} [MPa]	104,200

Table 5
Non-Schmid constants.

c_1	c_2	c_3	c_4
0.0	0.0	−0.03	−0.03

Table 6
Latent hardening parameters [27,124].

a_0	a_1	a_2	a_3	a_4	a_5
0.068	0.068	0.0454	0.625	0.137	0.122

Table 7
Contributing terms to the initial slip resistance ($\tau_0^s = \tau_{0,ss} + \tau_{0,HP}^s + \tau_{0,shear} + \tau_{0,loop} + \tau_{0,forest}$,) per material.

Slip resistance contribution	AM Vertical	AM Horizontal	AM Diagonal	AM + HIP	Wrought
$\tau_{0,forest}$ [MPa]	44.2	44.2	44.2	44.2	44.2
$\tau_{0,HP}^s$ [MPa]	60.7	76.6	76.3	31.5	37.4
$\tau_{0,shear}$ [MPa]	268.1	268.1	268.1	317.9	318.6
$\tau_{0,loop}$ [MPa]	1.1	1.1	1.1	2.0	0.9
$\tau_{0,ss}$ [MPa]	60.0	60.0	60.0	15.0	40.0
τ_0^s [MPa]	434.1	450.0	449.7	410.6	441.0

$$\mathbf{P}^s = \mathbf{P}_{sc}^s + \mathbf{P}_{ns}^s \tag{1d}$$

where τ_c^s is the slip resistance. The commonly used Schmid tensor (1c) is modified to include other stress projections (1 b), often referred to as the

Table 8
Comparison of measured 0.2% offset and simulated yield stress per material.

σ_y [MPa]	Vertical	Horizontal	Diagonal	AM + HIP	Wrought
Sim.-Comp.	1309	1358	1378	1261	1321
Exp.-Comp.	1255	1345	1370	1125	1205
Sim.-Tens.	1221	1264	1273	1190	1268
Exp.-Tens.	1215	1290	1305	1105	1170

non-Schmid effects [80,81]. The geometry of a slip system, s, is defined by a unit vector aligned with the Burgers direction, $\mathbf{b}^s$ and a unit vector aligned with the slip system plane normal, $\mathbf{n}^s$, and $\mathbf{t}^s = \mathbf{b}^s \times \mathbf{n}^s$. In the present study, we consider the FCC structure of IN718 alloy, for which, the crystallographic slips on $\{110\}\langle\bar{1}11\rangle$ systems i.e. their 12 positive s + and 12 negative s-directions are accommodating the imposed plastic strain. The parameter $\dot{\gamma}_0$ is a reference normalization factor (taken here to be 0.001/s) and n is the power-law exponent representing the inverse of the material strain rate-sensitivity (taken here to be 20). The term $\tau^s_{bs}(\mathbf{x})$ stands for the back-stress hardening and will be described later in this section. While the weighting coefficients c_1, c_2, c_3, c_4 can be obtained from experiments on single crystal, we obtain these coefficients by calibrating the calculated monotonic tension-compression stress--strain curves with the experimental measurements [21]. The c_1, c_2 coefficients have very slight effect in tension-compression asymmetry while c_3, c_4 constants play the major role in the asymmetry [80].

Hooke's law is used in EVPFFT to represent the constitutive relation between the work conjugated stress and strain measures:

$$\boldsymbol{\sigma}^{t+\Delta t}(\mathbf{x}) = \mathbf{C}(\mathbf{x})\,\boldsymbol{\varepsilon}^{e,t+\Delta t}(\mathbf{x}) = \mathbf{C}(\mathbf{x})\,(\boldsymbol{\varepsilon}^{t+\Delta t}(\mathbf{x}) - \boldsymbol{\varepsilon}^{p,t}(\mathbf{x}) - \dot{\boldsymbol{\varepsilon}}^{p,t+\Delta t}(\mathbf{x}, \boldsymbol{\sigma}^{t+\Delta t})\Delta t), \quad (2)$$

where $\mathbf{C}(\mathbf{x})$ is the elastic stiffness tensor in the sample frame calculated from the crystal elastic stiffness tensor using the transformation matrix of orientations [82–86], and $\boldsymbol{\varepsilon}(\mathbf{x})$ $\boldsymbol{\varepsilon}^e(\mathbf{x})$, and $\boldsymbol{\varepsilon}^p(\mathbf{x})$ are the total, elastic, and plastic strain tensors. Using Eq. (2), the total strain can be defined as

$$\boldsymbol{\varepsilon}^{t+\Delta t}(\mathbf{x}) = \mathbf{C}^{-1}(\mathbf{x})\,\boldsymbol{\sigma}^{t+\Delta t}(\mathbf{x}) + \boldsymbol{\varepsilon}^{p,t}(\mathbf{x}) + \dot{\boldsymbol{\varepsilon}}^{p,t+\Delta t}(\mathbf{x}, \boldsymbol{\sigma}^{t+\Delta t})\Delta t. \quad (3)$$

2.1. Summary of the full-field EVPFFT model

After adding and subtracting the stiffness of a reference linear medium, $\mathbf{C}^0$, from the Cauchy stress, we obtain

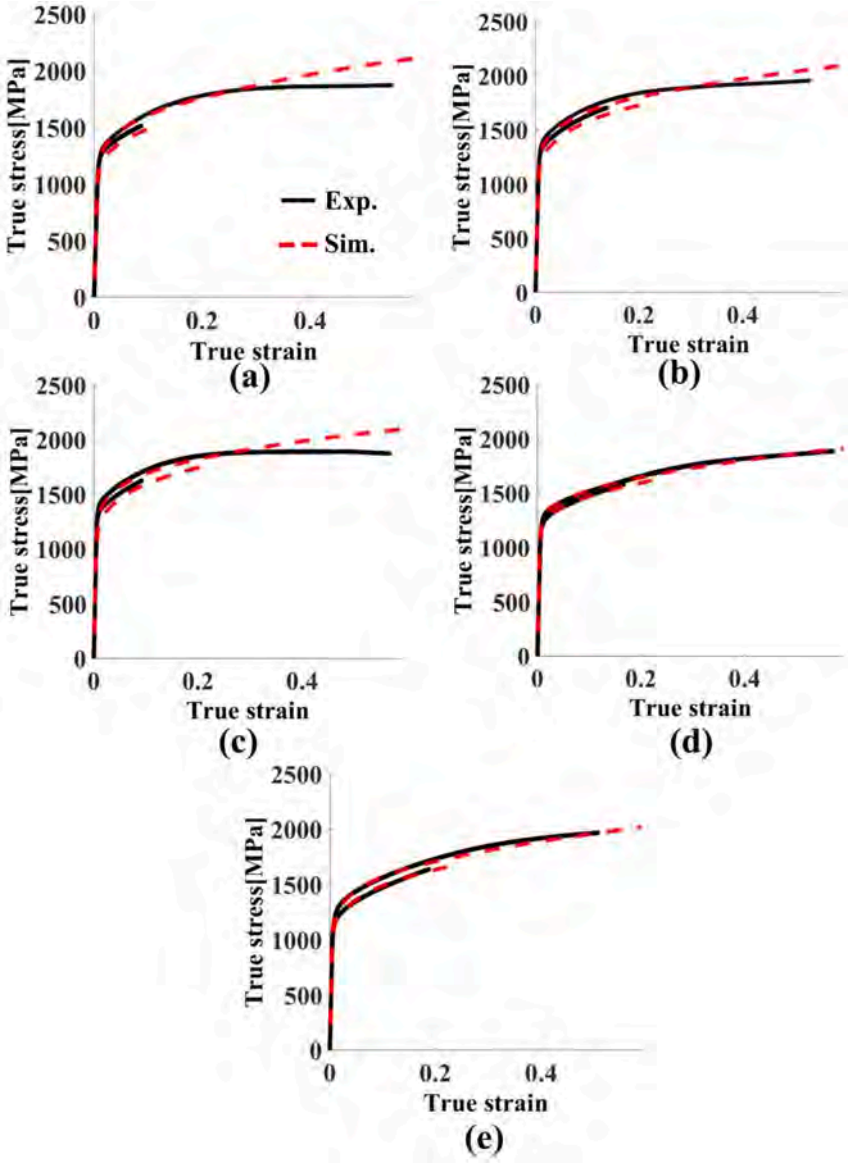

Fig. 4. Comparison of measured [21,63] and predicted response in tension (less strong shorter curves experimentally pulled to fracture) and compression (curves to large strains ~0.5) for samples of IN718: AM vertical, (b) AM horizontal, (c) AM diagonal, (d) Wrought, and (e) AM + HIP microstructures.

Table 9
Hardening parameters.

DD parameters	AM/AM + HIP	Wrought
$k_1\,[m^{-1}]$	7.0e8	4.0e8
$D\,[MPa]$	470	420
g	0.0425	0.0425
$\rho_{0,forest}\,[m^{-2}]$	1.0e13	1.0e13
H	0.55	0.55
q	0.1	0.1
$\mu_{IN718}\,[MPa]$	69.06	69.06

$$\sigma_{ij}(\mathbf{x}) = \sigma_{ij}(\mathbf{x}) + C^0_{ijkl}u_{k,l}(\mathbf{x}) - C^0_{ijkl}u_{k,l}(\mathbf{x}), \tag{4}$$

where $u_{k,l}(\mathbf{x})$ represents the displacement gradient tensor. Furthermore, we can write

$$\sigma_{ij}(\mathbf{x}) = C^0_{ijkl}u_{k,l}(\mathbf{x}) + \varphi_{ij}(\mathbf{x}), \tag{5}$$

with

$$\varphi_{ij}(\mathbf{x}) = \sigma_{ij}(\mathbf{x}) - C^0_{ijkl}u_{k,l}(\mathbf{x}), \tag{6}$$

where the term $\varphi_{ij}(\mathbf{x})$ represents the polarization field. Using the equilibrium equation $\sigma_{ij,j}(\mathbf{x}) = \mathbf{0}$, Eq. (5) becomes

$$C^0_{ijkl}u_{k,lj}(\mathbf{x}) + \varphi_{ij,j}(\mathbf{x}) = 0. \tag{7}$$

Using Green's approach for solving partial differential equations (PDEs) [87], Green's function $G_{km}(\mathbf{x})$ can be associated with the displacement field $u_k(\mathbf{x})$ as

$$C^0_{ijkl}G_{km,lj}(\mathbf{x} - \mathbf{x}') + \delta_{im}\delta(\mathbf{x} - \mathbf{x}') = \mathbf{0} \tag{8}$$

and the convolution theorem [88] to obtain the local displacement gradient fluctuation tensor

$$\tilde{u}_{k,l}(\mathbf{x}) = \int_{R^3} G_{ki,jl}(\mathbf{x} - \mathbf{x}')\varphi_{ij}(\mathbf{x}')\, d\mathbf{x}'. \tag{9}$$

Solving Eq. (9) in Fourier space and then performing the inverse transform to get back to the real space, we can represent the strain field around the average strain value, E_{ij}, using

$$\varepsilon_{ij}(\mathbf{x}) = E_{ij} + FT^{-1}\left(sym\left(\widehat{\Gamma}^0_{ijkl}(\mathbf{k})\right)\widehat{\varphi}_{kl}(\mathbf{k})\right) \tag{10}$$

where the symbols "$\widehat{\ }$" and FT^{-1} indicate direct and inverse Fourier transforms, respectively, and $\mathbf{k}$ is a point (frequency) in the Fourier Space. The fourth rank tensor $\widehat{\Gamma}^0_{ijkl}(\mathbf{k})$ is

$$\widehat{\Gamma}^0_{ijkl}(\mathbf{k}) = -k_j k_l \widehat{G}_{ik}(\mathbf{k});\ \widehat{G}_{ik}(\mathbf{k}) = \left[C_{kjil}k_l k_j\right]^{-1}. \tag{11}$$

Solution of Eq. (7) necessitates an iterative procedure to obtain the stress and strain field. If we consider $\lambda^{(i)}_{ij}$ and $e^{(i)}_{ij}$ to be the initial guess for the stress and strain fields, respectively, for equation Eq. (6) we have

$$\varphi^{(i)}_{ij}(\mathbf{x}) = \lambda^{(i)}_{ij}(\mathbf{x}) - C^0_{ijkl}e^{(i)}_{kl}(\mathbf{x}), \tag{12}$$

The next guess for the strain field is obtained using Eq. (10)

$$e^{(i+1)}_{ij}(\mathbf{x}) = E_{ij} + FT^{-1}\left(sym\left(\widehat{\Gamma}^0_{ijkl}(\mathbf{k})\right)\widehat{\varphi}^{(i)}_{kl}(\mathbf{k})\right). \tag{13}$$

In order to use directly the stress field rather than the polarization field, Eq. (13) can be written as [89].

$$e^{(i+1)}_{ij}(\mathrm{X}) = E_{ij} + FT^{-1}\left(\tilde{e}^{(i)}_{ij} + sym\left(\widehat{F}^0_{ijkl}(\mathrm{k})\right)\widehat{\lambda}^{(i)}_{kl}(\mathrm{k})\right) \tag{14}$$

An augmented Lagrangian scheme is utilized to minimize the suitably defined residual as a function of the stress tensor $\boldsymbol{\sigma}^{(i+1)}$ and strain tensor $\boldsymbol{\varepsilon}^{(i+1)}$ as [62].

$$R_k\left(\boldsymbol{\sigma}^{(i+1)}\right) = \sigma^{(i+1)}_k + C^0_{kl}\varepsilon^{(i+1)}_l\left(\boldsymbol{\sigma}^{(i+1)}\right) - \lambda^{(i)}_k - C^0_{kl}e^{(i+1)}_l \tag{15}$$

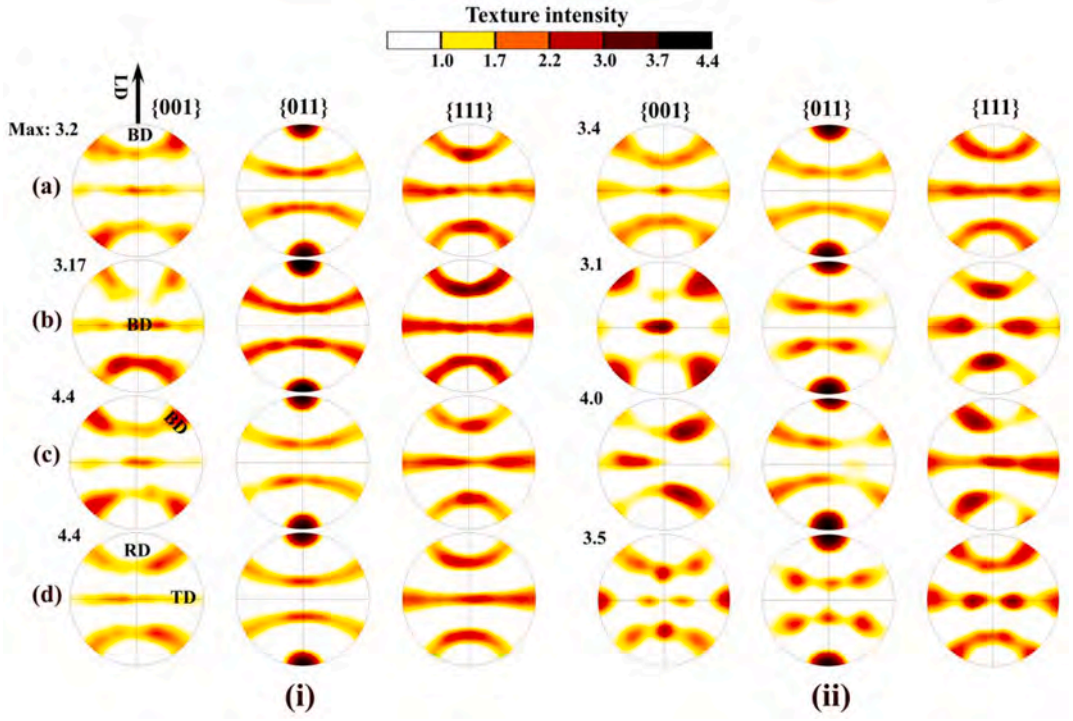

Fig. 5. Pole figures showing the comparison between (i) simulated and (ii) measured [28] texture evolution for: (a) AM vertical, (b) AM horizontal, (c) AM diagonal, and (d) AM + HIP materials at 0.55, 0.53, 0.57, and 0.57 strain levels, respectively.

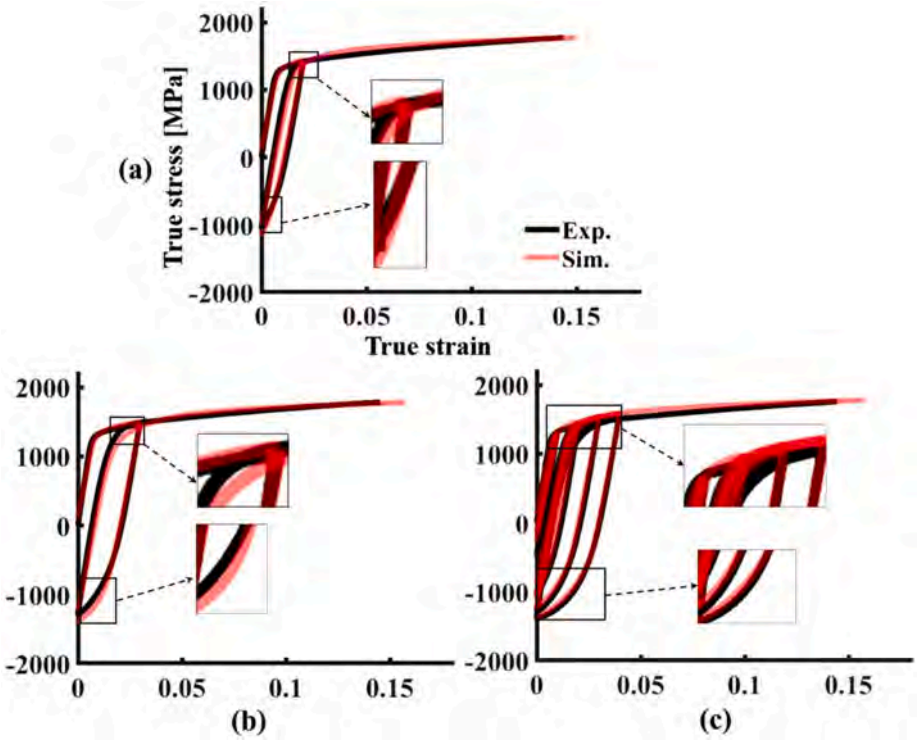

Fig. 6. Comparison of measured [27] and predicted load reversal responses for AM IN718: (a) AM Horizontal 2%, (b) AM Horizontal 3%, and (c) AM Horizontal 1-2-3-4%.

Advantages of the augmented Lagrange scheme have been discussed in Ref. [90,91]. It is chosen over other constrained minimization techniques because of exhibiting faster converge behavior in EVPFFT. In above equation, the Voigt notation has been used to express the symmetric tensors σ_{ij} and C_{ijkl} as vectors with

$$\begin{aligned} &\sigma_{ij}\rightarrow\sigma_k\ , \quad k=1,6 \\ &C_{ijkl}\rightarrow C_{kl}\ , \ k,l=1,6. \end{aligned} \tag{16}$$

Solving Eq. (15) using the Newton-Raphson (NR) method is

$$\sigma_k^{(i+1,j+1)}=\sigma_k^{(i+1,j)}-\left(\frac{\partial R_k}{\partial\sigma_l}\Big|\boldsymbol{\sigma}^{(i+1,j)}\right)^{-1}R_l\left(\boldsymbol{\sigma}^{(i+1,j)}\right), \tag{17}$$

$$\frac{\partial R_k}{\partial\sigma_l}\Big|\boldsymbol{\sigma}^{(i+1,j)}=\delta_{kl}+C_{kq}^0C_{ql}^{-1}+\Delta tC_{kq}^0\frac{\partial\dot{\varepsilon}_q^{\,p}}{\partial\sigma_l}\Big|\boldsymbol{\sigma}^{(i+1,j)}. \tag{18}$$

Since the slip resistance, $\tau_c^s(\mathbf{x})$, is a function of stress $\tau_c^s\left(\boldsymbol{\sigma}^{(i+1,j)}(\mathbf{x})\right)$, the term $\frac{\partial\dot{\varepsilon}_q^p}{\partial\sigma_l}|\boldsymbol{\sigma}^{(i+1,j)}$ is

$$\frac{\partial\dot{\varepsilon}_q^p}{\partial\sigma_l}\Big|\boldsymbol{\sigma}^{(i+1,j)}\cong n\dot{\gamma}_0\sum\nolimits_{s=1}^{N}\frac{P_q^sP_l^s}{\tau_c^s(\boldsymbol{\sigma}^{(i+1,j)}(\mathbf{x}))}\left(\frac{\mathbf{P}^s(\mathbf{x})\cdot\boldsymbol{\sigma}(\mathbf{x})-\tau_{bs}^s}{\tau_c^s(\boldsymbol{\sigma}^{(i+1,j)}(\mathbf{x}))}\right)^{n-1}. \tag{19}$$

Incorporating Eq. (19) into Eq. (18) gives

$$\frac{\partial R_k}{\partial\sigma_l}\Big|\boldsymbol{\sigma}^{(i+1,j)}\cong\delta_{kl}+C_{kq}^0C_{ql}^{-1}+\left(\Delta t\ n\ \dot{\gamma}_0\right)C_{kq}^0\sum\nolimits_{s=1}^{N}\frac{P_q^sP_l^s}{\tau_c^s(\boldsymbol{\sigma}^{(i+1,j)}(\mathbf{x}))}\left(\frac{\mathbf{P}^s(\mathbf{x})\cdot\boldsymbol{\sigma}(\mathbf{x})-\tau_{bs}^s}{\tau_c^s(\boldsymbol{\sigma}^{(i+1,j)}(\mathbf{x}))}\right)^{n-1}. \tag{20}$$

where $\sigma_k^{(i+1j+1)}$ is the (j+1) guess for stress field $\sigma_k^{(i+1)}$. Note that "j" enumerates the NR stress iterations. Coupling Eq. (3) and Eq. (17) results in finding the Jacobian

Table 10
Back-stress fitting parameters.

ν	600.0
A_{bs}	6.5
γ_b	0.01
$\tau_{bs}^{sat}[MPa]$	100.0

Minimizing the residual R_k by the iterative NR method, the solution for stress at each FFT point is obtained as the next guess for Eq. (12) and Eq. (14). The procedure continues until convergence to a pre-defined tolerance (TOL_{NR}) for each single crystal stress is reached

$$\frac{\left(\sigma_k^{(i+1,j+1)}-\sigma_k^{(i+1,j)}\right)\left(\sigma_k^{(i+1,j+1)}-\sigma_k^{(i+1,j)}\right)}{\sqrt{\lambda_{ij}^{(i)}\lambda_{ij}^{(i)}}}\prec TOL_{NR}=10^{-6} \tag{21}$$

The number of iterations for the case studies performed in this work given the exponent n and the tolerances is in the range from 3 to 6, which is consistent with the original code [62].

The stress and strain field tolerance (TOL_{stress_field} , TOL_{strain_field}) after solving Eq. (15) are

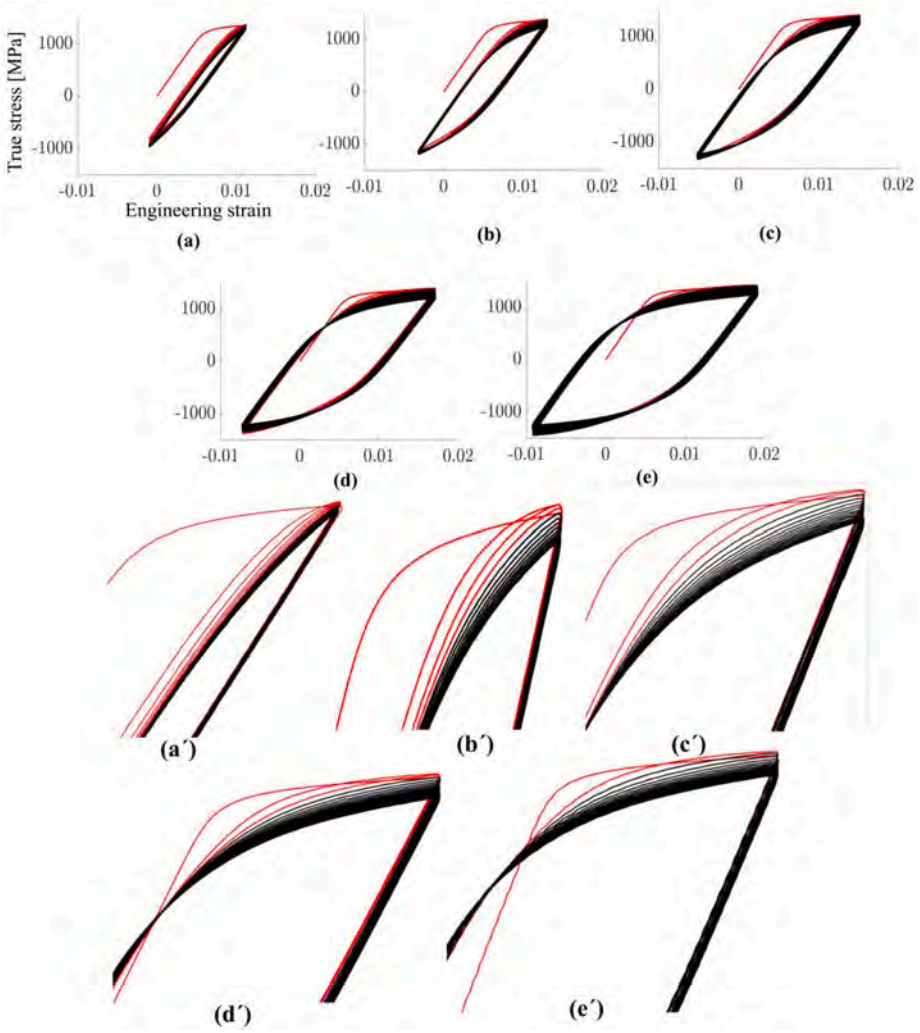

Fig. 7. Stress-strain hysteresis loops for AM diagonal LCF samples of IN718 at engineering strain amplitudes of: (a) 0.6%, (b) 0.8%, (c) 1.0%, (d) 1.2%, and (e) 1.4% [10]. Cyclic hardening is plotted with red color, while cyclic softening is plotted with black color. (For interpretation of the references to color in this figure legend, the reader is referred to the Web version of this article.)

$$\left.\frac{\left\langle\left(\sigma_k^{(i+1)}-\lambda_k^{(i)}\right)\left(\sigma_k^{(i+1)}-\lambda_k^{(i)}\right)\right\rangle}{\sqrt{\frac{3}{2}\Sigma_{ij}^{'(i)}\Sigma_{ij}^{'(i)}}} \prec TOL_{stress\_field}=10^{-6}\right) \tag{22a}$$

$$\frac{\left\langle\left(\varepsilon_k^{(i+1)}-e_k^{(i)}\right)\left(\varepsilon_k^{(i+1)}-e_k^{(i)}\right)\right\rangle}{\sqrt{\frac{2}{3}E_{ij}^{'(i)}E_{ij}^{'(i)}}} \prec TOL_{strain\_field}=10^{-6} \tag{22b}$$

where $\langle\rangle$ indicates volume average and $\Sigma_{ij}^{'}$ and $E_{ij}^{'}$ denote the deviatoric stress and strain of the polycrystal. These are also calculated by averaging the corresponding local quantities

$$\Sigma_{ij}^{'}=\frac{\sum_{X,Y,Z}\left(\sigma_{ij}^{'}(\mathbf{x})\right)}{N^3}\ ;\ N=\#of\ voxels\ in\ X,Y,Z,$$
$$E_{ij}^{'}=\frac{\sum_{X,Y,Z}\left(\varepsilon_{ij}^{p}(\mathbf{x})\right)}{N^3}\ . \tag{23}$$

The number of iterations over the field for the case studies performed in this work is about 20 for the given tolerances, which is also consistent with the original code [62].

2.2. Dislocation density-based hardening law within EVPFFT

We further develop a statistically stored dislocation density-based hardening law that we had incorporated into the EVPFFT model in our recent work [64] to enable strengthening effects due to grain size and shape, solid solution, shearing of small precipitates, and Orowan looping around larger precipitates. The rate of dislocation storage is a thermally activated process, which is dependent on temperature and strain-rate. Evolution of the resistance to slip per slip system, s, consists of

$$\tau_c^s=\tau_0^s+\tau_{shear}+\tau_{forest}^s+\tau_{deb}. \tag{24a}$$

$$\tau_0^s=\tau_{0,ss}+\tau_{0,HP}^s+\tau_{0,shear}+\tau_{0,loop}+\tau_{0,forest}, \tag{24b}$$

The initial resistance to slip, τ_0^s, incudes a solid solution term, $\tau_{0,ss}$, the Hall-Petch-like barrier term, $\tau_{0,HP}^s$, shearing term $\tau_{0,shear}$, looping term, $\tau_{0,loop}$, and a term, which is a consequence of any initial content of forest dislocations, $\rho_{0,forest}$. The Hall-Petch-like term is defined using [27].

$$\tau_{0,HP}^s=\frac{H\mu_{IN718}\sqrt{b_{INC718}}}{\sqrt{d_{mfp}^s}}, \tag{25a}$$

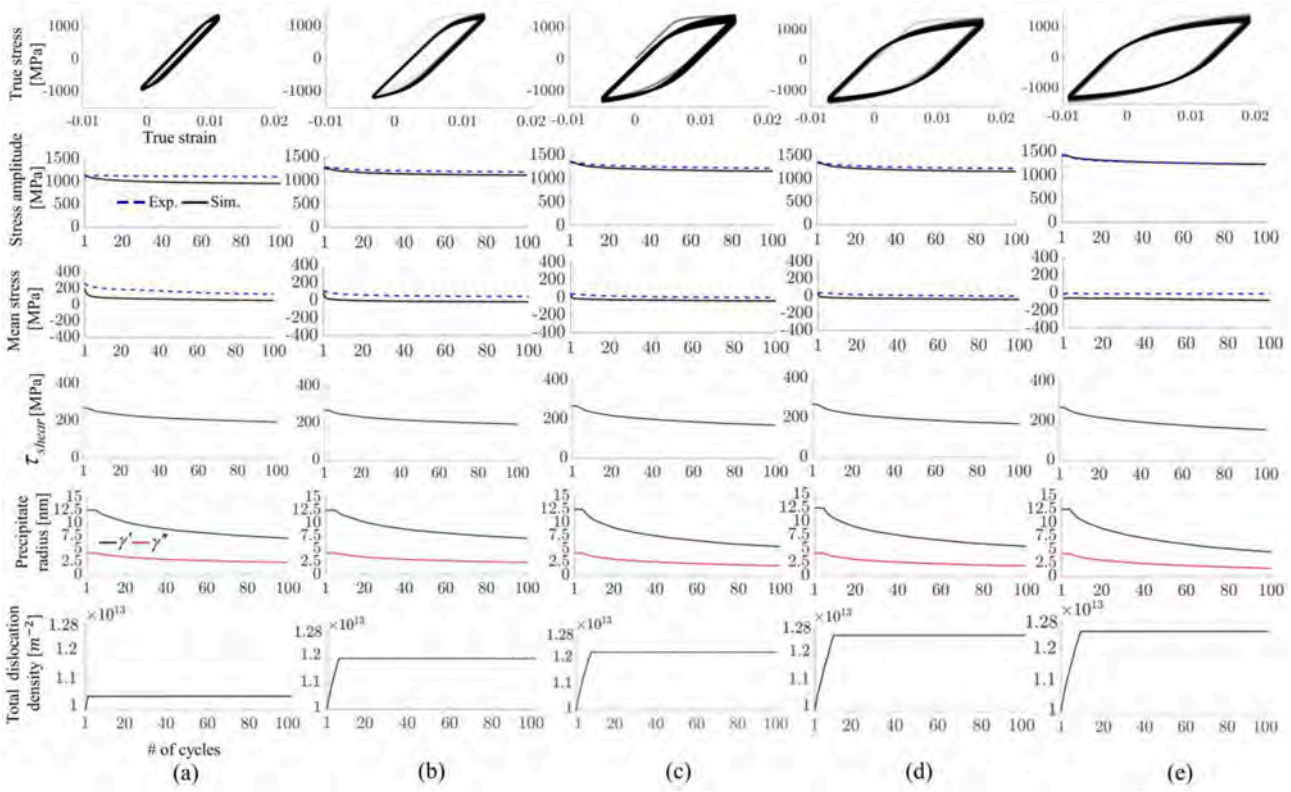

Fig. 8. Evolution of stress-amplitudes, mean stress, radii of precipitates, contribution to the slip resistance due to shearing of the precipitates, and dislocation density with cycles for AM diagonal samples of IN718 at strain amplitudes of: (a) 0.6%, (b) 0.8%, (c) 1.0%, (d) 1.2%, and (e) 1.4%.

$$d^s_{mfp} = \frac{2}{\sqrt{\left(\frac{\widehat{b}^s_x}{a}\right)^2 + \left(\frac{\widehat{b}^s_y}{b}\right)^2 + \left(\frac{\widehat{b}^s_z}{c}\right)^2}}, \tag{25b}$$

where b_{IN718}, μ_{IN718}, and H are the Burgers vector, shear modulus, and Hall-Petch fitting coefficient, respectively. The parameters a, b, and c represent the local ellipsoidal grain shape, while $\widehat{b}^s_x$, $\widehat{b}^s_y$ and $\widehat{b}^s_z$ define the Burgers vector direction facilitating the calculation of the mean-free-path, d^s_{mfp}, per slip system s.

The symbol $\tau_{0,shear}$ represents the initial value of the precipitate shear resistance for the initial precipitate fraction and size. The shear term evolves with precipitate cutting, which is an operative softening mechanism during cyclic deformation. The shear resistance for shearable γ' and γ'' precipitates is [26,92].

$$\tau_{shear} = 0.7\left(\mu_{\gamma'}\left(\frac{APB_{\gamma'}}{\mu_{\gamma'} b_{\gamma'}}\right)^{\frac{3}{2}}\left(\frac{f_{\gamma'} r_{\gamma'}}{b_{\gamma'}}\right)^{\frac{1}{2}} + \mu_{\gamma''}\left(\frac{APB_{\gamma''}}{\mu_{\gamma''} b_{\gamma''}}\right)^{\frac{3}{2}}\left(\frac{f_{\gamma''} r_{\gamma''}}{b_{\gamma''}}\right)^{\frac{1}{2}}\right) \tag{26}$$

where $APB_{\gamma'}$ and $APB_{\gamma''}$ are the antiphase boundary energies, $f_{\gamma'}$ and $f_{\gamma''}$ are the volume fractions, and $r_{\gamma'}$ and $r_{\gamma''}$ are the average radii of the precipitates γ' and γ'', respectively. The parameters μ and b stand for shear modulus and Burgers vector, respectively. Note that negligible fraction of δ and MC phases might be sheared, which is disregarded.

The Orowan looping-induced shear resistance, $\tau_{0,loop}$, occurs for large particles of δ and MC phases [26]. The looping resistance is

$$\tau_{0,loop} = \frac{\mu_\delta b_\delta}{\bar{l}_\delta} + \frac{\mu_{MC} b_{MC}}{\bar{l}_{MC}} = \alpha\left(\mu_\delta b_\delta \frac{f_\delta}{r_\delta(1-f_\delta)} + \mu_{MC} b_{MC}\frac{f_{MC}}{r_{MC}(1-f_{MC})}\right), \tag{27a}$$

where $\bar{l}$ stands for mean spacing between particles. The fitting parameter $\alpha = 1.1719$ is estimated for IN718 based on a reported value for IN100 in Ref. [26]. This is done by relating the particle size and volume fraction of looping phase in718 to those of IN100 as following

$$\bar{l} = \sqrt{\frac{2\pi}{3\bar{f}}}\bar{r},\ \alpha \propto \frac{1}{\bar{l}};\ \left[\bar{r}_{IN718} = \frac{r_\delta + r_{MC}}{2}, \bar{f}_{IN718} = \frac{f_\delta + f_{MC}}{2}\right]$$
$$\frac{\bar{l}_{IN100}}{\bar{l}_{IN718}} = \frac{\bar{r}_{IN100}}{\bar{r}_{IN718}}\sqrt{\frac{\bar{f}_{IN718,loop}}{\bar{f}_{IN100,loop}}}, \frac{\alpha_{IN100}}{\alpha_{IN718}} = \frac{\bar{l}_{IN718}}{\bar{l}_{IN100}}. \tag{27b}$$

The average precipitate size and volume fraction are estimates as the average of those quantities for δ and MC precipitates provided in Table 2.

The term $\tau_{0,ss}$is the solid solution contribution to the initial slip resistance which is estimated using the initial slip resistance calibration.

The evolution of slip resistance owing to the evolution of statistically stored dislocations is [93–95].

$$\tau^s_{forest} = b_{IN718}\chi\,\mu_{IN718}\sqrt{\rho^s_{tot} + L^{ss'}\sum_{s\neq s'}\rho^{s'}_{tot}}, \tag{28}$$

where, b_{IN718} represents the burgers vector of IN718, χ denotes the dislocation interaction parameter taken to be 0.9 [96,97]. The magnitude of the χ parameter was reported to be in the range 0.04–2.6 and depends on crystal structure, strain rate, temperature, and alloying [96]. The chosen value is consistent with our earlier works [27,98–100] and in agreement with [101,102]. $L^{ss'}$ is the latent hardening interaction matrix provided in appendix A for FCC crystals.

Total dislocation density is split into two dislocation populations to facilitate modeling of strain-path changes, one termed as forward and another termed as reversible [103]. Thus, the total dislocation density is

$$\rho^s_{tot} = \rho^s_{forw} + \rho^{s+}_{rev} + \rho^{s-}_{rev} \tag{29}$$

where ρ^s_{forw} is the forward dislocation density, while ρ^{s+}_{rev} and ρ^{s-}_{rev} are

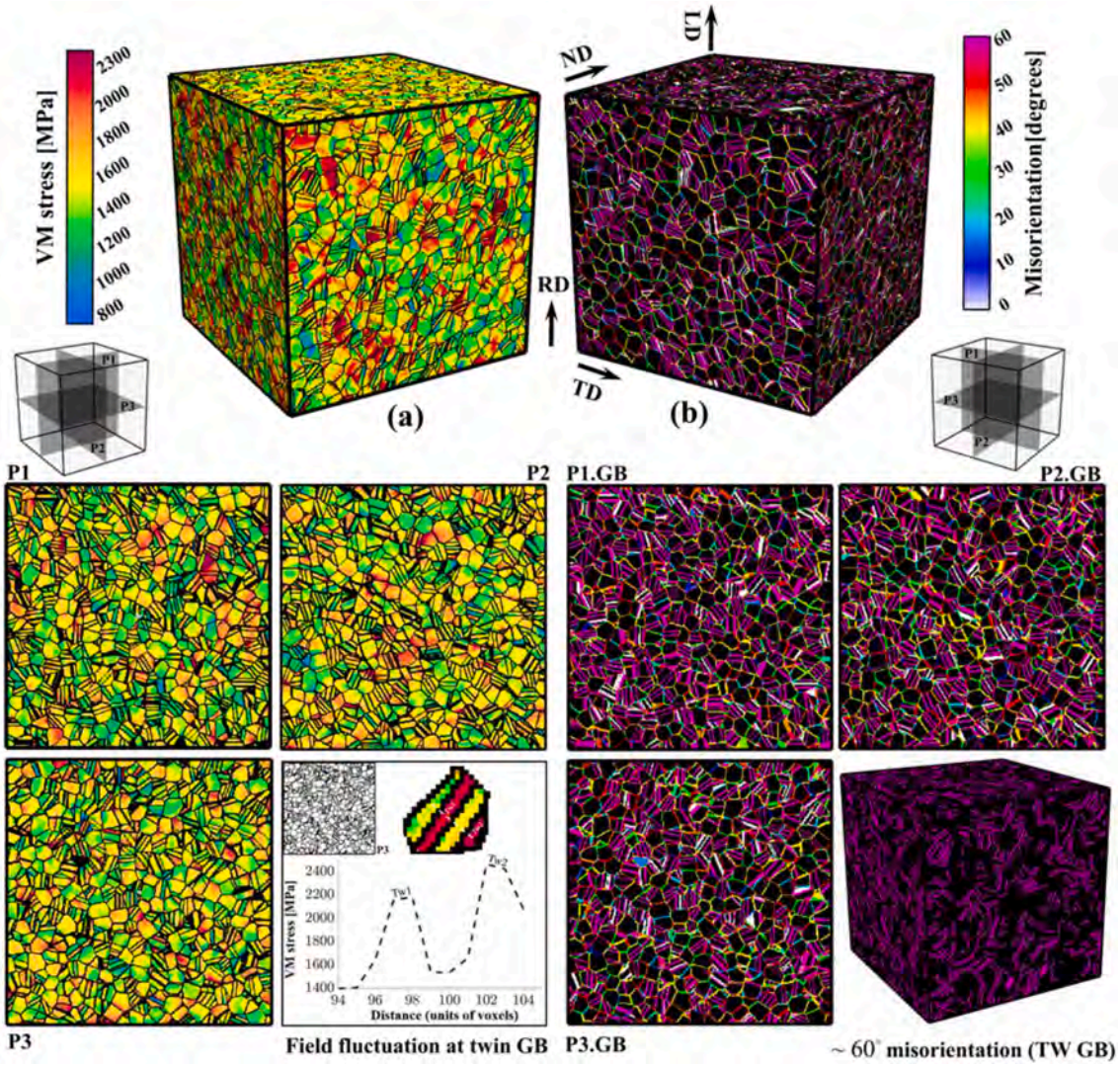

Fig. 9. (a) Contours of von Mises stress after simple compression to a strain of 1% over a microstructural cell for wrought IN718. (b) Misorientation distribution at the grain boundaries revealing coherent twins with misorientation of 60° relative to the parent grain.

reversible dislocation densities on the slip directions s^+ and s^-, respectively. The forward dislocation density is driven by competition between the rate of storage and the rate of dynamic recovery [94,97,104].

$$d\gamma^{s+} > 0 \ : \ \frac{\partial \rho^s_{forw}}{\partial \gamma^s} = (1-p)k_1\sqrt{\rho^s_{forw}+\rho^{s+}_{rev}} - k_2(\dot{\varepsilon},T)\rho^s_{forw}, \tag{30a}$$

$$d\gamma^{s-} > 0 \ : \ \frac{\partial \rho^s_{forw}}{\partial \gamma^s} = (1-p)k_1\sqrt{\rho^s_{forw}+\rho^{s-}_{rev}} - k_2(\dot{\varepsilon},T)\rho^s_{forw}, \tag{30b}$$

where k_1 is a fitting constant governing the generation. The coefficient k_2 is the rate sensitivity constant governed by the dynamic recovery [105]. The parameter p is the shear reversibility factor in the range 0–1. The factor separates the portion of forward and reversible populations within the total dislocation population. At low to moderate strain levels, $p = 1$. In contrast, at large plastic strains the dislocation substructures/debris can obstruct the reversible motion causing $p \leq 1$ [103]. The reversibility parameter of $p = 1$ indicated that entire dislocation population is prone to gliding in the opposite direction under load reversal. As the plastic strains in the present work is relatively low, especially in LCF, a value of $p = 1$ is taken for the reversibility parameter. The stored reversible dislocations are dependent on the direction of shearing as

if $d\gamma^{s+} > 0$:

$$\frac{\partial \rho^{s+}_{rev}}{\partial \gamma^s} = pk_1\sqrt{\rho^s_{forw}+\rho^{s+}_{rev}} - k_2(\dot{\varepsilon},T)\rho^{s+}_{rev}, \tag{31a}$$

$$\frac{\partial \rho^{s-}_{rev}}{\partial \gamma^s} = -k_1\sqrt{\rho^s_{forw}+\rho^{s+}_{rev}}\left(\frac{\rho^{s-}_{rev}}{\rho^s_{tot}}\right)^m, \tag{31b}$$

if $d\gamma^{s-} > 0$:

$$\frac{\partial \rho^{s-}_{rev}}{\partial \gamma^s} = pk_1\sqrt{\rho^s_{forw}+\rho^{s-}_{rev}} - k_2(\dot{\varepsilon},T)\rho^{s-}_{rev}, \tag{31c}$$

$$\frac{\partial \rho^{s+}_{rev}}{\partial \gamma^s} = -k_1\sqrt{\rho^s_{forw}+\rho^{s-}_{rev}}\left(\frac{\rho^{s+}_{rev}}{\rho^s_{tot}}\right)^m, \tag{31d}$$

with :

$$\rho^{s+}_{rev}|_{t=0} = \rho^{s-}_{rev}|_{t=0} = 0, \ \rho^s_{forw}|_{t=0} = \rho_{0,forest}$$

where, the power m controls the rate of dislocation recombination and is taken here as 0.5 [106]. The parameter $k_2(\dot{\varepsilon},T)$ is calculated using

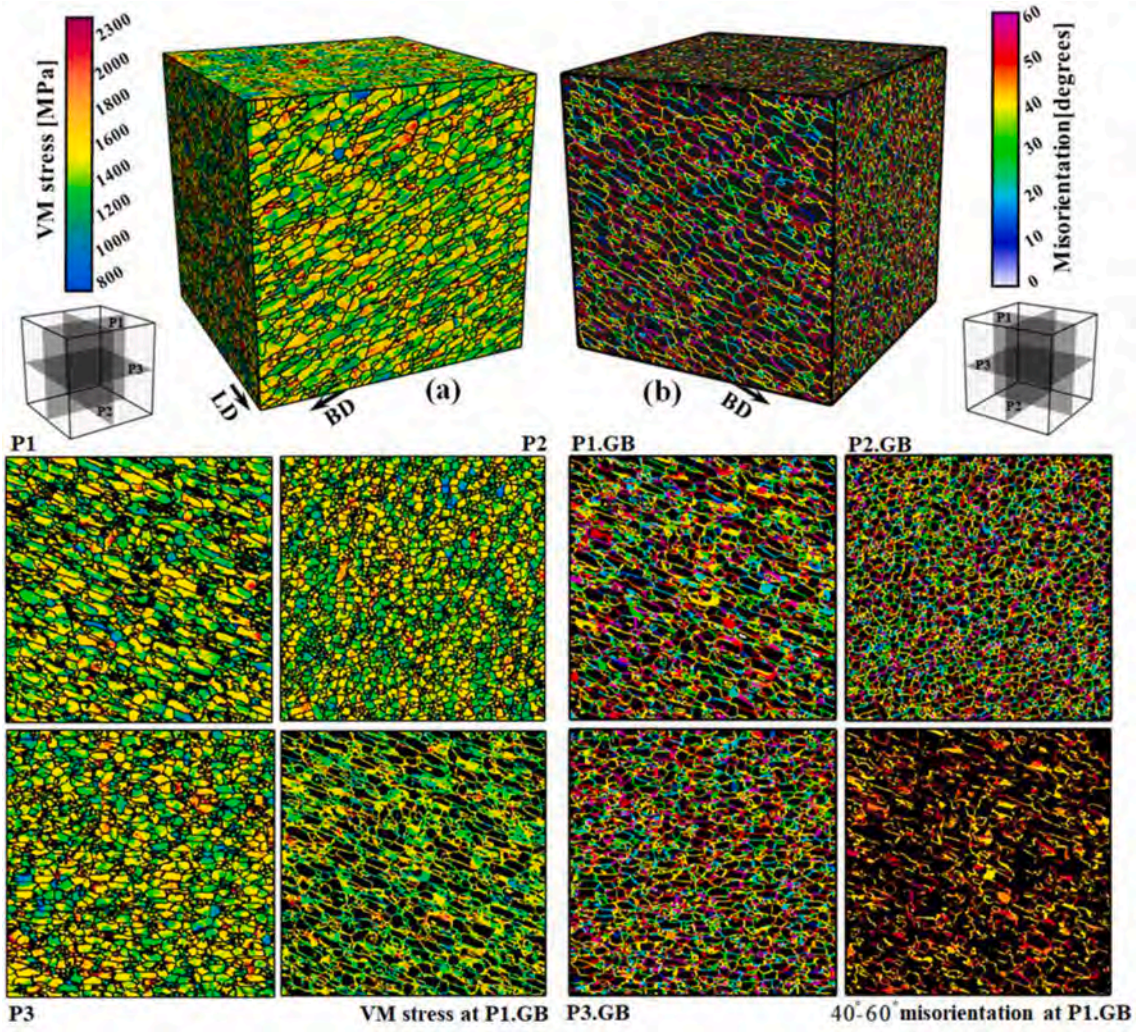

Fig. 10. (a) Contours of von Mises stress after simple compression to a strain of 1% over a microstructural cell for AM + HIP IN718. (b) Misorientation distribution at the grain boundaries revealing incoherent twins with misorientation of 60° relative to neighboring grains.

$$k_2 = \frac{k_1 \chi b_{IN718}}{g}\left(1 - \frac{k_B T}{D(b_{IN718})^3}\ln\left(\frac{\dot{\varepsilon}}{\dot{\varepsilon}_0}\right)\right), \tag{32}$$

where g is an activation enthalpy, k_B is the Boltzmann constant, $\dot{\varepsilon}_0$ is a reference strain-rate taken to be 10^7 s^{-1}, and D is a drag stress.

The debris term, τ_{deb}, is a driven by the debris/substructure dislocations [107] as

$$\tau_{deb} = 0.086\,\mu_{IN718} b_{IN718}\sqrt{\rho_{deb}}\log\left(\frac{1}{b_{IN718}\sqrt{\rho_{deb}}}\right), \tag{33}$$

where, ρ_{deb} is the debris dislocation population. The evolution of debris density follows

$$d\rho_{deb} = \sum_s q b_{IN718}\sqrt{\rho_{deb}} k_2(\dot{\varepsilon}, T)\rho^s_{tot}|d\gamma^s| \tag{34}$$

The parameter q is a parameter fit to separate the population of removed dislocations ($\frac{\partial \rho^s_{rem,tot}}{\partial \gamma^s} = k_2(\dot{\varepsilon}, T)\rho^s_{tot,}$) to form debris/substructures and set to be 0.1.

Eq. (34) is based on the thermally activated processes, such as cross slip and climb, which are responsible for pattern formation [102, 108–112]. These processes are responsible for the recovery of dislocations. However, in this model, a small fraction of the recovered forest dislocations contribute to substructure development. The substructure density is used to model later stages in hardening. The formulation, however, neglects the length-scales and pattern-types associated with substructure.

2.3. Back-stress at the slip system level

The strain gradients within and in between grains with crystallographic contrast (i.e. soft vs hard grains) [113] is accommodated by geometrically necessary dislocations (GNDs), which are sources of localized hardening and back-stress fields [114]. Moreover, hard particles/precipitates in the microstructure cause the dislocations to bow (loop) around them rather than cutting through them. The new length of dislocations after looping around the hard particles necessitates GNDs accommodated by strain gradient plasticity [92]. Strain gradients of plastic slip govern the GND density which in turn governs the back-stress field [115]. Such strain gradient plasticity formulations have been developed within the full-field crystal plasticity solvers [115–118]. In particular, an EVPFFT formulation has recently been extended to a phenomenological mesoscale field dislocation mechanics in order to tackle plastic flow and hardening due to GND density distributions [117, 118]. In this formulation and in contrast with the present paper, a Hall-Petch law at the intra-crystalline level was not introduced and slip gradients due to GND density pile ups were found to be responsible for grain size effect of the Hall-Petch type at the macroscopic level. A modified Kocks-Mecking's law with GND densities was used in contrast

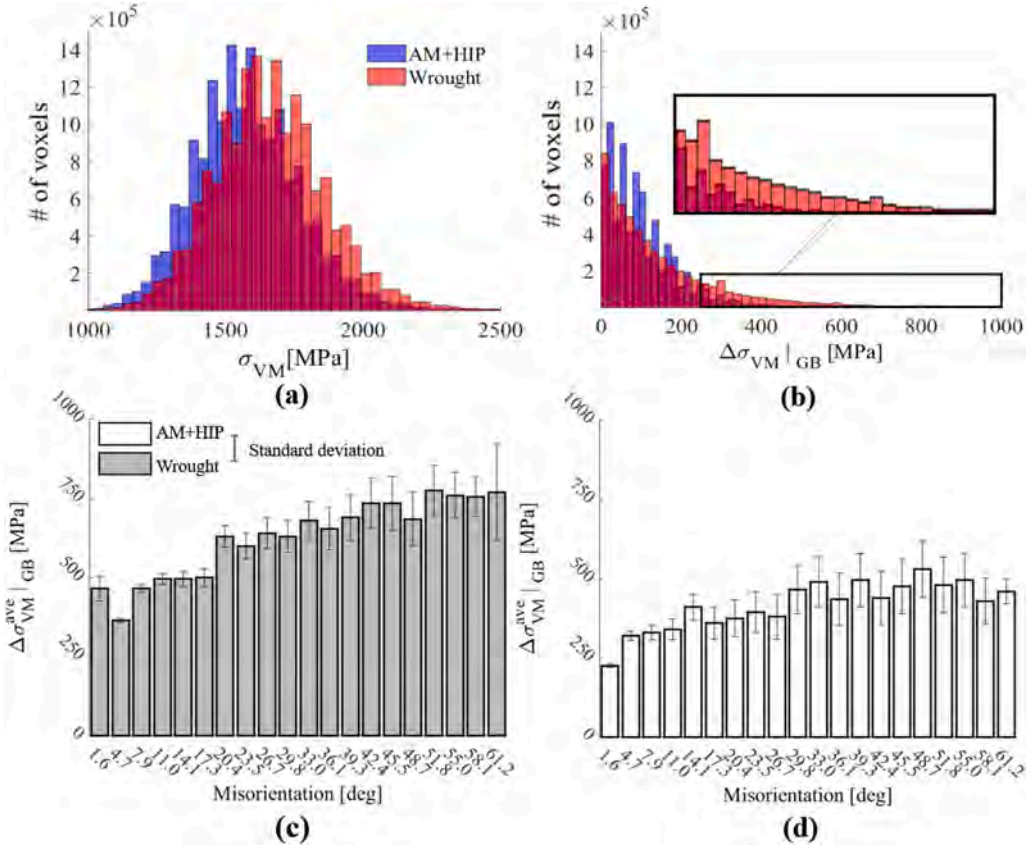

Fig. 11. (a) Frequency of von Mises stress field within RVEs. (b) Frequency of stress gradient across GBs for AM + HIP and wrought microstructures. Variation of average stress gradient versus misorientation at GBs for (c) wrought material and (d) AM + HIP material.

with conventional strain-hardening as used in Eqs. (30) and (31). However, due to significant difficulties with such formulations, a phenomenological approach is adopted here to approximate the evolution of back-stress fields by fitting the data. The adopted approach is a simplification of the actual physical phenomena but is relatively simple and importantly computationally efficient.

The evolution law for the slip system level back-stress helping or hindering the deformation of a crystal consists of the following equations given an increment in shear $d\gamma^{s+/-} > 0$ (whether in the forward + or in the reverse – direction) [64].

if $\tau_{bs,sys}^{s+/-} > 0$:

$$^{*}\gamma^{s+/-} = \frac{-1}{\nu}\ln\left(1 - \frac{\tau_{bs,sys}^{s+/-}}{\tau_{bs}^{sat}}\right), \tag{35a}$$

$$\tau_{bs,sys}^{s+/-} = \tau_{bs}^{sat}\left(1 - \exp\left(-\nu\left(^{*}\gamma^{s+/-} + d\gamma^{s+/-}\right)\right)\right),$$
$$\tau_{bs,sys}^{s-/+} = -A_{bs}\tau_{bs,sys}^{s+/-}, \tag{35b}$$

elseif $\tau_{bs,sys}^{s+/-} < 0$:

$$^{**}\gamma^{s+/-} = -\gamma_b \ln\left(\frac{\tau_{bs}^{sat} - \tau_{bs,sys}^{s+/-}}{(A_{bs}+1)\tau_{bs}^{sat}}\right), \tag{35c}$$

$$\tau_{bs,sys}^{s+/-} = -(A_{bs}+1)\tau_{bs,sys}^{s+/-}\exp\left(-\frac{^{**}\gamma^{s+/-} + d\gamma^{s+/-}}{\gamma_b}\right) + \tau_{bs}^{sat},$$
$$\tau_{bs,sys}^{s-/+} = -\frac{1}{A_{bs}}\tau_{bs,sys}^{s+/-}, \tag{35d}$$

where $\tau_{bs,sys}^{s+/-}$ is back-stress at the slip system-level for s^+ and s^-. A_{bs} and ν are the back-stress parameters fit using macroscopic data. Additionally, the saturation, τ_{bs}^{sat}, is another fitting parameter. The slip level kinematic hardening mimics the local plasticity governing non-linear unloading and the Bauschinger effect. While $\tau_{bs}^{s^+}$ acts opposite to the resolved shear stress on s^+, i.e. $\mathbf{P}^{s^+}\cdot\boldsymbol{\sigma} - \tau_{bs}^{s^+} = \tau_c^s$, signaling that $\tau_{bs}^{s^+}$ lowers the resolved shear stress, $\tau_{bs}^{s^-}$ aids the resolved shear stress on s^-: $\mathbf{P}^{s^-}\cdot\boldsymbol{\sigma} - \tau_{bs}^{s^-} = \tau_c^s$. The respective effect of local incompatibility stresses (predicted by the full field model) compared to the effect of the intra-granular back-stress on predicting the particularities pertaining to the cyclic response have been studied in our earlier work [64]. The finding was that the inclusion of the back-stress term is essential.

3. Microstructure and texture of alloy IN718 in AM, AM + HIP, and wrought forms

MPI-ACC-EVPCUFFT utilizes a uniform grid of FFT sampling points in 3D (i.e. voxels) to discretize microstructural grain structures. Grain structures in 3D can be measured using experimental techniques such as focused ion beam electron backscattered diffraction (FIB-EBSD) [119] and post-processed into voxels or generated synthetically. Since measured data for the alloys studied in the present work are not available, the structures are generated synthetically. In doing so, it is attempted to mimic the features observed in EBSD scans per microstructure as closely as possible. This included preparing statistical input for DREAM.3D in terms of grain shapes and sizes (elongated vs equiaxed), grain aspect ratios, volume fraction of phases, precipitate fractions, and twin regions (twin volume fractions and thickness of twinned areas). As DREAM3D works based on such statistical input to generate synthetic microstructures, it inevitably obscures the exact structures

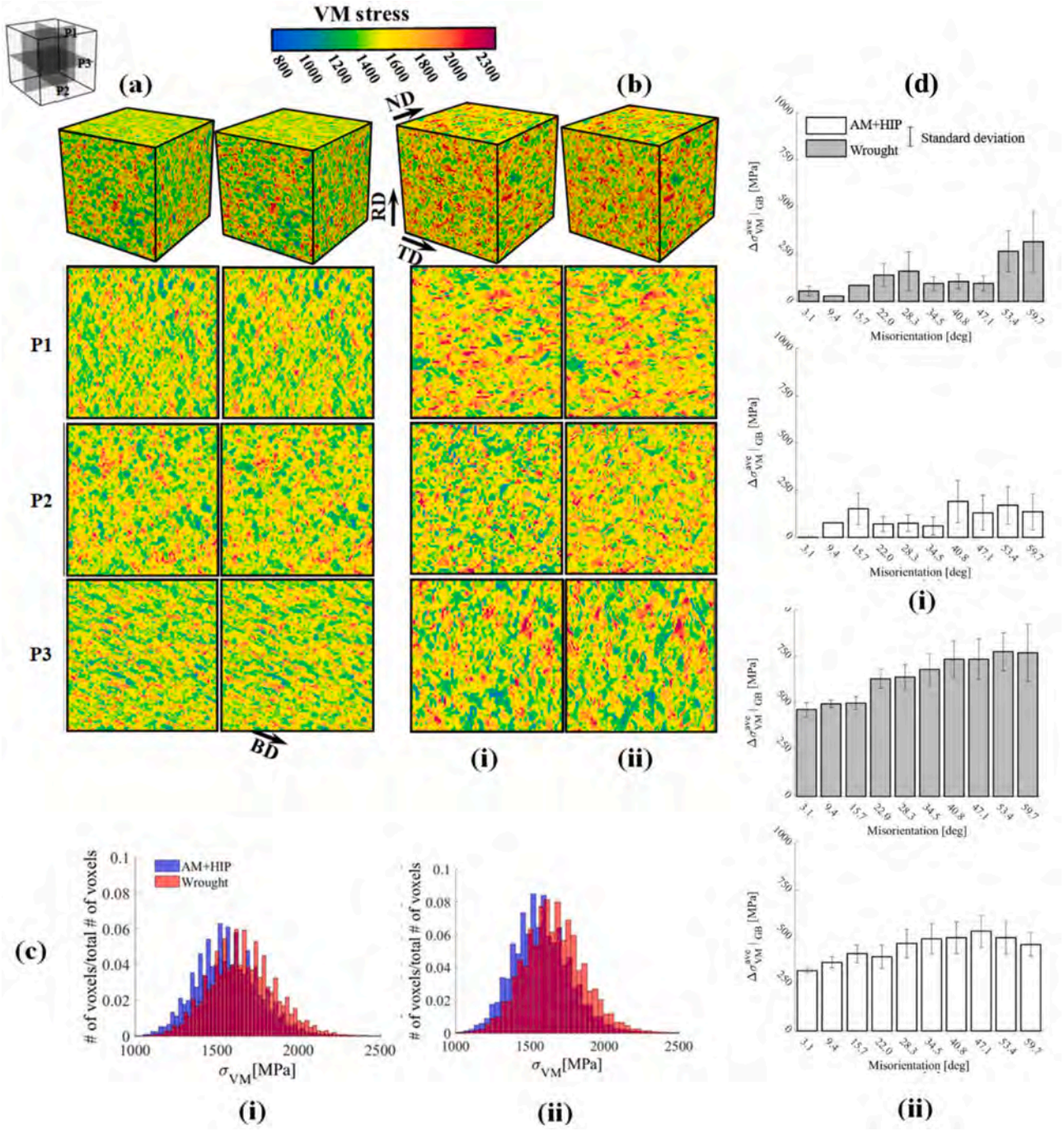

Fig. 12. Contours of von Mises (VM) stress after simple compression to a strain of 1% over the microstructural cell (RVE) for (a) AM + HIP and (b) wrought IN718 as a function of resolution: (i) 64^3, and (ii) 256^3. (c) Frequency of von Mises stress field within the RVEs. (d) Variation of average stress gradient versus misorientation at GBs for the RVEs.

while matching them in the statistical sense.

Fig. 1 shows microstructural cells or RVEs (representative volume elements) for AM horizontal, AM vertical, AM diagonal, AM + HIP, and wrought IN718 samples. The images are the IPF (inverse pole figure) color map of 256^3 resolution. Lower resolution of 64^3 microstructural cells were also created to facilitate simulations to very high number of increments like in LCF. Since these images whether 256^3 or 64^3 were indistinguishable, 64^3 resolution microstructures are not shown. The cells are prepared based on statistical data of microstructural features presented in Refs. [21,63]. Consistent with the data, the wrought material contains 36% coherent twins of 60° misorientation relative to the parent grains, while the AM + HIP material has 33% of incoherent twins, which are also misoriented 60°. The grains in the AM materials are elongated in the AM build direction (BD), while the wrought material has them equiaxed. Table 1 provides the required information input into DREAM3D to generate such synthetic RVEs. Upon creating grain morphologies, measured crystallographic textures are assigned to the structures. To do so, an ODF correspond to each microstructure is read from an ascii file using DREAM3D (odf import) and then assigned to the RVE features by an interpolation procedure of the software. Moreover, for the twinned microstructures, in order to ensure the correct orientation relationship between the twinned region and parent grains, we relied on the "insert transformation phases" pipeline of the software, in which the transformation phase misorientation, habit plane, and

Table 11
Hardware specs of the NH BioMade supercomputer.

Cluster	# of nodes	Compiler	OS	CPU	GPU	# of GPUs per node	CUDA toolkit version	System memory (GB)	# of CPUs	# of threads per core	# of sockets	# of cores per socket
NH BioMade	4	PGI v 2019 v19.7	Centos 7.6	Intel(R) Xeon(R) Gold 6130 CPU @ 2.10 GHz	NVIDIA Tesla V100 (32 GB)	1	10.1	800	32	2	2	16

Table 12
Simulation benchmarks on NH BioMade supercomputer.

Deformation type	Strain	RVE resolution	Wall clock time (hrs)
Monotonic compression	0.53 (true strain)	64^3	0.66
Monotonic tension	0.14 (true strain)	64^3	0.023
LCF	100 cycles, 1.4% strain amplitude	64^3	6.42
High resolution fields (AM + HIP)	0.01 (true strain)	256^3	5.06
High resolution fields (Wrought)	0.01 (true strain)	256^3	4.92

transformation phase thickness are explicitly defined. Pole figures showing texture per material are provided in Fig. 2.

Considering that microstructural simulations in 3D can offer insights into the effect of grain structure on micromechanical fields, a grain boundary detection algorithm is developed. In particular, we explore the ability of the model to predict discontinuities in the fields across grain boundaries (GBs) including the coherent/incoherent annealing twin-parent grain boundaries, which are known to play an important role in crack nucleation during fatigue loading. To this end, a search algorithm is developed to find the neighbor voxels for any two adjacent grains.

While DREAM3D generates the microstructure RVEs for the EVPFFT model input, it does not generate GBs. To create the GBs and in order to facilitate visualizing GBs and monitoring the properties at voxels across the GBs, a standalone MATLAB code is developed to generate the grain boundaries for the EVPFFT model. The GB algorithm performs a search over the entire microstructure RVE and finds neighbor voxels. As soon as two neighbors are found to carry different grain IDs, they are stored as grain boundary voxels. Once the GBs are found, their correspond data is appended to the original EVPFFT input generated by DREAM3D and converted to "H5part" output [120]. The conversion to "H5part" is necessary for efficient I/O and post-processing of high-resolution RVEs (i.e. 256^3 voxels) in ParaView [121]. Appendix B provides a schematic of the neighbor search and grain boundary detection. The GB search algorithm finds the GBs based on the voxelized output "Export Los Alamos FFT file" from DREAM3D. We acknowledge that a more sophisticated composite voxel strategy has been developed in Ref. [122] to better resolve the interface between adjacent grains. An implementation of such strategy in our solver will be explored in the future research.

As intensity of the textures is relatively weak (Fig. 2), the effect of grain shape/size is expected to be more important in governing the difference in behavior of the given microstructure. Since the grain morphologies are oriented differently relative to the loading axis, an effective measure for the grain size/shape is used to represent the morphology effects on the anisotropy of mechanical behavior. The effective grain shape is described by an ellipsoid with major a and minor b or c axes representing the average grain morphology per microstructure. Fig. 3 schematically shows the effect of elongated grain morphology on mean-free-path per AM microstructure. Eq. (25) is used to calculate the dislocation mean-free-path entering the barrier contribution to the slip resistance.

4. Results and discussion

4.1. Monotonic response

Calibration of the MPI-ACC-EVPCUFFT model for alloy IN718 starts by predicting yield stress for five microstructures against the corresponding experimental measurements. The material exhibits moderate anisotropy and tension-compression asymmetry originating from microstructure. Microstructural features relevant to the resistance to slip estimates are given in Table 2. Volume fractions of the precipitates are taken from the recent characterization work of the same materials [23],

while sizes are estimated based on the data and literature survey presented in Refs. [21,23,27]. The APB energies for shearable precipitates are taken from Ref. [27]. Finally, morphological features from the studied materials are taken from Ref. [21] and are summarized in Table 3. These features give rise to the Hall-Petch barrier effect. Given these microstructural features per material and the initial microstructural cells, it is possible to estimate resistance to slip and yield stress for every material. Table 4 presents the crystal elastic constants for IN718 [123]. To promote tension-compression asymmetry, non-Schmid constants have been estimated as presented in Table 5, while the latent hardening parameters are given in Table 6 [124]. Tables 7 and 8 present estimated slip resistances and predicted yield stresses per material. Except the solid solution contribution to the slip resistance, the other terms are predictions based on microstructure. The solid solution term is adjusted to ensure the predictions of yield stress per material. As is evident, the contribution of the looping term is secondary. Estimation of yield stress by MPI-ACC-EVPCUFFT is accomplished by disabling any hardening i.e. performing perfectly plastic simulations. Comparison of the measured and predicted yield stress values per material revealed that the grain structure, with minor contribution of crystallographic texture, governs plastic anisotropy of the alloy, while non-Schmid effects promote the tension-compression asymmetry.

Calculations pertaining to the hardening behavior under compression and tension are shown in Fig. 4. Table 9 provides the fitting parameters used for dislocation density hardening law for IN718. While a single set of parameters are used for AM materials, a slightly different values for the initial hardening slope and drag stress are found to improve the fits for the wrought material. The chemical composition of the powder used in AM was presented in Ref. [63], while the exact composition of wrought IN718 was not measured/known. As specifications for the alloy composition allow some variation i.e. certain elements must be within min/max bounds [125], we associate a slight difference in the parameters to any potential difference in the compositions between AM and wrought materials. Three curves are used in fitting (AM vertical, AM + HIP, and wrought), while the remaining two can be regarded as predictions. In order to capture the monotonic response, the following parameters associated with the hardening laws are fit: the Hall-Petch constant, the rate coefficient, k_1, the activation barrier, g, the drag stress, D, and another rate coefficient q. Upon the initial slip resistance has been estimated as explained above to predict the initial yield stress, the fitting procedure of the hardening parameters beyond yielding starts with varying, k_1, such that the initial hardening slope is reproduced. Next, g and D are fit to match the subsequent hardening rate. Finally, q is adjusted to reproduce hardening at the later stages of plastic strain. While tensile response is predicted well for all materials, the predictions at strains larger than 0.3 in compression are poor for the AM materials, likely because defects not considered by the model such as voids influence the large strain hardening response of these materials. As plastic deformation proceeds to large plastic strains, defects in the structure develop. Flattening of the true stress – true strains curves for the AM samples is an indication of damage processes meaning that hardening is hardly keeping up with generation of defects. Generation of defects in the AM samples is enhanced by existing voids in the AM structures. Size and distribution of voids in the materials were presented in Ref. [21,63]. Since the synthetic grain structures used in the modeling were fully dense, the effects of voids on damage processes were not modeled. Moreover, the constitutive model does not incorporate a damage criteria to enable capturing of damage formation and growth for modeling of softening and eventual failure. Fig. 5 shows the predicted texture evolution in comparison with experiments for compression. Formation of the {011} fiber is well predicted. These results indicates that the developed model can capture anisotropy and tension-compression asymmetry during monotonic loading as well as the underlying texture/microstructure evolution for the studied materials with good accuracy.

4.2. Load reversal response

The model is further adjusted and verified to predict load reversal data. Here, particularities pertaining to such deformation are linear followed by non-linear unloading upon the load reversal, the Bauschinger effect (BE), and change in the hardening rate from that achieved during the forward loading. Fig. 6 presents the comparison between measured and predicted load reversal response for AM IN718. The experimental data is from Refs. [27]. To achieve such predictions, the back-stress law was adjusted. The following parameters are fit: parameters ν and γ_b, saturation value for back-stresses τ_{bs}^{sat}, and asymmetry factor, A. Table 10 presents these parameters. Good predictions of large strain cyclic deformation provide incentive to attempt predicting LCF behavior of the material.

4.3. LCF

The MPI-ACC-EVPCUFFT model verified on monotonic and load reversal data is used to predict the LCF behavior of the material without further adjustment of the material parameters. Accordingly, the hardening parameters (Table 9) and the back-stress parameters (Table 10) are used for the LCF simulations. However, as LCF behavior of IN718 is governed by a combination of dislocation mechanisms (generation and annihilations) and precipitate shearing. The effects of the later mechanism need to be considered by the model.

Fig. 7 shows the LCF data under strain amplitudes of 0.6%, 0.8%, 1.0%, 1.2% and 1.4% for AM diagonal IN718 at room temperature taken from Refs. [10]. The data shows short hardening (red) followed by prolonged softening (black). According to the data, the cycle at which transition from hardening to softening occurs, is dependent on the strain amplitude. The lowest strain amplitude (i.e. 0.6%) experiences higher number of hardening hysteresis loops before the softening initiates. The transition cycle from hardening to softening are determined to be 6, 4, 3, 3, 2 cycles (red) for strain amplitudes of 0.6%, 0.8%, 1.0%, 1.2% and 1.4%, respectively. Dislocation are likely generated during cyclic hardening, while likely annihilated or remain constant during cyclic softening. The added mechanism controlling the LCF behavior is the refinement of precipitates.

In the model, we allow dislocation density to increase only during cyclic hardening, while the density remains constant upon the transition to cyclic softening. Density of dislocations in LCF increases initially when plasticity takes places, while it remains constant or decreases during subsequent cycling. The latter is physically justified by either the rate of dislocation generation is equal to the rate of annihilation or the same dislocations move back and force during cycling. As such no cyclic softening will be obtained. In order to achieve cyclic softening, we rely on the mechanism of precipitate shearing and resulting size reduction.

The LCF data is simulated using the MPI-ACC-EVPCUFFT model. In doing so, the evolution of precipitate size is adjusted to achieve the fits. In particular, the evolution of shear term is controlled to achieve the stress amplitude and mean stress consistent with the experimental data. Knowing the shear term values, the precipitate sizes $r_{\gamma'}$ and $r_{\gamma''}$ can be solved for using Eq. (26). Fig. 8 presents the simulation results in terms of several variables with the number of cycles of up to 100: stress amplitude, mean stress, precipitate radius, shearing term of slip resistance, and total dislocation density. In these simulations, the precipitate radius is inferred, while the stress amplitudes are fit per strain amplitude. Thus, the key outcome of the simulations is the inference of precipitate radius for γ' and γ'' with cycles and the underlying evolution of shearing term resistance.

4.4. Mechanical fields

We now turn our attention from macroscopic response to mechanical fields over the microstructure. The MPI-ACC-EVPCUFFT simulation

framework facilitate the examination of such fields over the voxel-based microstructural cells. In particular, we focus on the field fluctuations at GBs, and especially in the vicinity of annealing twin boundaries, which are known to nucleate cracks during fatigue [126,127]. While the actual crack nucleation is left for future work, the examples presented here reveal useful gradients in the fields likely responsible for crack nucleation.

As wrought and AM-HIP samples contain coherent and incoherent 60^0 misorientation boundaries, simulations to a strain of 1% in simple compression are performed using the high-resolution microstructural cells discretized with 256^3 voxels for these two materials. Figs. 9 and 10 illustrate the von Mises stress fields over the cells correlated with the grain boundary misorientstions. The first row of the figures shows the 3D distribution of fields, while the 2D slices are provided for a better illustration. Note that, the black voxels belong to grains but visualize GBs. The area of a plane cutting through GB voxels is rendered as black in the contours. The contour plots show that annealing twins, when geometrically and crystallographically oriented relative to the LD, can create sharp gradients in stress. The low and high stress states on either side of the coherent twin is due to the activated slip systems parallel to the twin boundary slip system of $\{111\}1\bar{1}0$. This allows the dislocations to travel long distances, creating high contrast of stress incompatibility at the twin GB [127,128]. Moreover, the 60^0 misorientation introduces a high crystallographic contrast in material properties between the parent grain and the twin children. This abrupt variation in stress, which in case of fatigue loading alternates frequently, expedites the crack initiation and failure in the wrought material [129].

Examination of the microstructural response for the AM + HIP material in Fig. 10a reveals the similar observations as for the wrought microstructure, however, since the twins are incoherent grain boundaries, the stress distribution is visualized over the grain boundaries as well to see the effect of GB misorientation on the localized stress within GBs. By relating the stress distribution across the GBs to the misorientation distribution we find that stress hotspots occur at grain boundaries with $40^\circ - 60^\circ$ misorientation. However, the gradients are not as sharp as in the wrought material.

Comparing the fields for AM + HIP and wrought materials reveals fields with lower magnitudes and lower gradient in the AM + HIP material. Such observations are better visualized in Fig. 11 versus misorientation. The histogram on top shows the frequency of the von Mises stress field for both AM + HIP and wrought microstructures. We find that wrought material experiences higher level of stress over larger number of voxels, since the material is stronger than AM + HIP. We also evaluate the distribution the local gradients across GBs for adjacent grains (neighbors). We observe that wrought microstructure experience higher level of the gradient, especially at the twin-parent GBs. Fig. 12 shows the effect of resolution on predicting the local mechanical fields. As is evident, the resolution of 64^3 shows very different results for the gradient across grain boundaries even though the homogenized macroscopic behavior is predicted well [64]. The loss of accuracy is attributed in part to grain boundaries loosing proper geometry and becoming thicker with lowering the resolution. A more sophisticated grain boundary detection methodology such as the one presented in Refs. [122] may relax the issue. In summary, to study mechanical fields at grain boundaries, an RVE resolution of at least 256^3 is recommended.

5. Computational efficiency of MPI-ACC-EVPCUFFT

In closing, we show the computational efficiency of the MPI-ACC-EVPCUFFT solver running on a high-performance cluster available at the University of New Hampshire (NH BioMade supercomputer). Table 11 provides the hardware specification of this cluster. The GPUs being utilized on the supercomputer for our simulations are the most advanced Nvidia Tesla V100 (32 GB) computing GPUs. The simulations are run on 4 Nvidia Tesla V100 GPUs installed on 4 distributed nodes. This is done by MPI + OpenACC parallelization developed earlier in Ref. [1]. Table 12 shows the computational time involved in monotonic deformation (compression and tension), LCF deformation, and high-resolution (256^3) field localization simulations. Each of 4 GPUs simulates a quarter of RVE with data chunk of $256 \times 256 \times 64$ voxels. Preforming the simulations on up to 256 GPUs is feasible in case of accessibility to such hardware configuration. The scalability of multi-GPU simulations are almost perfect. That is to say, increasing the number of GPUs by factor of N will decrease the computational time reported in Table 12 by factor of $\frac{1}{N}$ (e.g. 50% improved efficiency by doubling the number of GPUs). The capability of the code running on multiple GPUs enables us to simulate large polycrystalline data sets in order of few hours. To the authors' knowledge, the MPI-ACC-EVPCUFFT solver is a unique high performance full-field crystal plasticity implementation for computationally efficient polycrystal plasticity modeling. The authors have presented GPU implementations of other codes in Refs. [130,131].

6. Summary and conclusions

The effective and local behavior of the polycrystalline alloy IN718 in several manufacturing conditions is studied through a set of numerical simulations of voxel-based microstructural cells. The microstructural cells consistent with the measured microstructures are synthetically constructed to initialize the model setups for predicting mechanical behavior of the alloy. In particular, the experimentally measured microstructural features including grain size and shape and texture, and content of annealing twins are included in the cells. Variation in the microstructural features in the samples manufactured differently such as the distribution of grain size and shape, crystallographic texture, content of annealing twins, and precipitates among the samples facilitated reliable calibration and validation of model parameters. Since physically based, the model has a relatively small number of fitting parameters in comparison to the macroscopic models. Significantly, a single set of material parameters is established to model a range of IN718 microstructures. The capability of the model to reproduce both the texture evolution and mechanical response in terms of anisotropy, tension/compression asymmetry, non-linear unloading upon the load reversal, the Bauschinger effect, and reverse hardening for the alloy as a function of the microstructures is demonstrated. Moreover, it is demonstrated that the model predicts accurately the evolution of the stress–strain hysteresis loops with the number of cycles, as well as the mean stress relaxation and the cyclic hardening/softening observed in the LCF experiments.

By comparing the data and model predictions, it is reveals that the initial grain size and shape govern anisotropy of the material, which is captured using a Hall-Petch type relation involving a dislocation mean-free-path measure. Next, the tension-compression asymmetry results from the modified relation for the slip system activation, while the secondary effects come from the latent hardening. Finally, evolution of the shearing term resistance with the average radius of precipitates is the key to predicting the transition from cyclic hardening to cyclic softening. Furthermore, the simulations based on the high-resolution microstructural cells facilitated the discussion of the mechanical fields induced by annealing twins. Here, the annealing twin boundaries are predicted to cause large gradients in the mechanical fields. The wrought microstructure featuring a large fraction of coherent twins has larger stress levels than the HIP microstructure featuring a large fraction of incoherent twin boundaries. Such gradients are potential crack incubation cites.

The developed micromechanical model will be advanced in future works to predicting localizations, while the critical mechanical fields to assess the effect of cyclic deformation on the "hot spots" in the microstructure providing the link between the microstructure and the fatigue response can be calculated by the developed model. Through the

comprehensive modeling of alloy IN718, we have shown that, in addition to being predictive with good accuracy, the key advantage of MPI-ACC-EVPCUFFT lies in its computational efficiency, versatility, and flexibility to be adapted for other materials exhibiting complex deformation behavior.

CRediT authorship contribution statement

Adnan Eghtesad: Formal analysis, Investigation, Software, Validation, Visualization, Writing - review & editing. **Marko Knezevic:** Conceptualization, Funding acquisition, Methodology, Project administration, Resources, Supervision, Writing - original draft, Writing - review & editing.

Declaration of competing interest

The authors declare that they have no known competing financial interests or personal relationships that could have appeared to influence the work reported in this paper.

Acknowledgments

This research is sponsored by the U.S. National Science Foundation and accomplished under the CAREER grant no. CMMI-1650641. A. E. also acknowledges support from the Dissertation Year Fellowship (DYF) program at the University of New Hampshire (UNH).

Appendix C. Supplementary data

Supplementary data to this article can be found online at https://doi.org/10.1016/j.msea.2020.140478.

Appendix A

The symmetric latent hardening interaction matrix for FCC materials where $A_2, A_3, A_6, B_2, B_4, B_5, C_1, C_3, C_5, D_1, D_4$ and D_6 are the slip systems where A, B, C and D represent the $(\bar{1}11), (111), (\bar{1}\bar{1}1)$ and $(1\bar{1}1)$ slip planes. Index numbers 1 to 6 denote the $[011], [0\bar{1}1], [101], [\bar{1}01], [\bar{1}10]$ and $[110]$ slip directions. The constants $a_0, a_1, a_2, a_3, a_4, a_5$ for IN718 material are provided in Table 6.

	A_2	A_3	A_3	B_2	B_4	B_5	C_1	C_3	C_5	D_1	D_4	D_6
A_2	a_0	a_1	a_1	a_3	a_4	a_4	a_2	a_4	a_5	a_2	a_5	a_4
A_3		a_0	a_1	a_4	a_2	a_5	a_4	a_3	a_4	a_5	a_2	a_4
A_6			a_0	a_4	a_5	a_2	a_5	a_4	a_2	a_4	a_4	a_3
B_2				a_0	a_1	a_1	a_2	a_5	a_4	a_2	a_4	a_5
B_4					a_0	a_1	a_5	a_2	a_4	a_4	a_3	a_4
B_5						a_0	a_4	a_4	a_3	a_5	a_4	a_2
C_1							a_0	a_1	a_1	a_3	a_4	a_4
C_3								a_0	a_1	a_4	a_2	a_5
C_5									a_0	a_4	a_5	a_2
D_1										a_0	a_1	a_1
D_4											a_0	a_1
D_6												a_0

Appendix B

A schematic of gain boundary detection is shown in Fig. B1 Fig. B1. A pair of neighbor grains with different IDs are considered to be the grain boundaries. The grain boundary generation and data conversion to H5part format for efficient visualization in ParaView are performed as part of the algorithm. The H5part provides an application programming interface (API) that facilitates I/O and post-processing of large data-sets very efficiently.

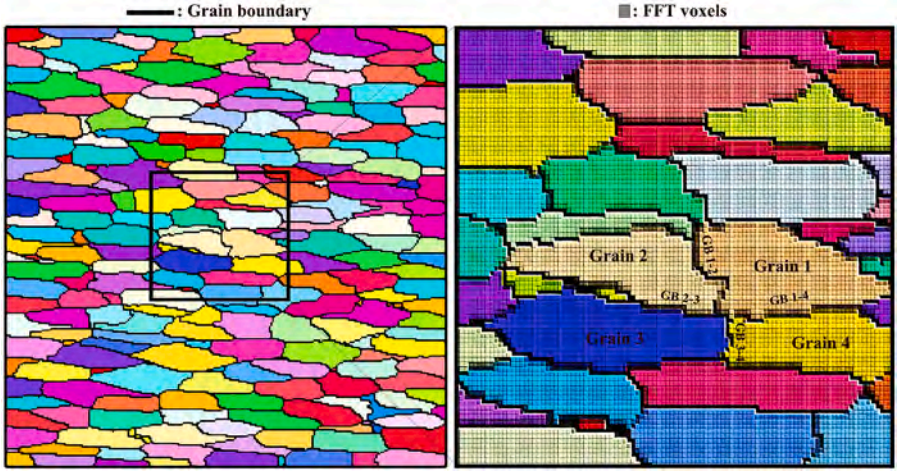

Fig. B1. A schematic of gain boundary detection.

Data availability

The raw/processed data required to reproduce these findings cannot be shared at this time due to technical or time limitations.

References

[1] A. Eghtesad, K. Germaschewski, R.A. Lebensohn, M. Knezevic, A multi-GPU implementation of a full-field crystal plasticity solver for efficient modeling of high-resolution microstructures, Comput. Phys. Commun. (2020) 107231.
[2] E.M. Francis, B.M.B. Grant, J.Q.d. Fonseca, P.J. Phillips, M.J. Mills, M. R. Daymond, M. Preuss, High-temperature deformation mechanisms in a polycrystalline nickel-base superalloy studied by neutron diffraction and electron microscopy, Acta Mater. 74 (2014) 18–29.
[3] G.A. Rao, M. Kumar, M. Srinivas, D. Sarma, Effect of standard heat treatment on the microstructure and mechanical properties of hot isostatically pressed superalloy inconel 718, Mater. Sci. Eng. 355 (2003) 114–125.
[4] C. Slama, M. Abdellaoui, Structural characterization of the aged Inconel 718, J. Alloys Compd. 306 (2000) 277–284.
[5] C.M. Kuo, Y.T. Yang, H.Y. Bor, C.N. Wei, C.C. Tai, Aging effects on the microstructure and creep behavior of Inconel 718 superalloy, Mater. Sci. Eng. 510–511 (2009) 289–294.
[6] Y. Mei, Y. Liu, C. Liu, C. Li, L. Yu, Q. Guo, H. Li, Effects of cold rolling on the precipitation kinetics and the morphology evolution of intermediate phases in Inconel 718 alloy, J. Alloys Compd. 649 (2015) 949–960.
[7] M. Knezevic, B.K. Chun, J.Y. Oh, W.T. Wu, R.A. Ress Iii, M.G. Glavicic, S. Srivatsa, Modeling Machining Distortion Using the Finite Element Method: Application to Engine Disk, in, 2012, pp. 40–46.
[8] N.C. Ferreri, S. Ghorbanpour, S. Bhowmik, R. Lussier, J. Bicknell, B.M. Patterson, M. Knezevic, Effects of build orientation and heat treatment on the evolution of microstructure and mechanical properties of alloy Mar-M-509 fabricated via laser powder bed fusion, Int. J. Plast. 121 (2019) 116–133.
[9] K. Amato, S. Gaytan, L. Murr, E. Martinez, P. Shindo, J. Hernandez, S. Collins, F. Medina, Microstructures and mechanical behavior of Inconel 718 fabricated by selective laser melting, Acta Mater. 60 (2012) 2229–2239.
[10] S. Gribbin, J. Bicknell, L. Jorgensen, I. Tsukrov, M. Knezevic, Low cycle fatigue behavior of direct metal laser sintered Inconel alloy 718, Int. J. Fatig. 93 (2016) 156–167. Part 1.
[11] K. Yuan, W. Guo, P. Li, Y. Zhang, X. Li, X. Lin, Thermomechanical behavior of laser metal deposited Inconel 718 superalloy over a wide range of temperature and strain rate: testing and constitutive modeling, Mech. Mater. 135 (2019) 13–25.
[12] H. Wang, A. Dhiman, H.E. Ostergaard, Y. Zhang, T. Siegmund, J.J. Kruzic, V. Tomar, Nanoindentation based properties of Inconel 718 at elevated temperatures: a comparison of conventional versus additively manufactured samples, Int. J. Plast. 120 (2019) 380–394.
[13] S. Sui, J. Chen, E. Fan, H. Yang, X. Lin, W. Huang, The influence of Laves phases on the high-cycle fatigue behavior of laser additive manufactured Inconel 718, Mater. Sci. Eng. 695 (2017) 6–13.
[14] C. Wang, R. Li, Effect of double aging treatment on structure in Inconel 718 alloy, J. Mater. Sci. 39 (2004) 2593–2595.
[15] S. Ghosh, S. Yadav, G. Das, Study of standard heat treatment on mechanical properties of Inconel 718 using ball indentation technique, Mater. Lett. 62 (2008) 2619–2622.
[16] J.R. Davis, ASM Specialty Handbook: Heat-Resistant Materials, ASM International, 1997.
[17] L. Xiao, M. Chaturvedi, D. Chen, Low-cycle fatigue behavior of INCONEL 718 superalloy with different concentrations of boron at room temperature, Metall. Mater. Trans. 36 (2005) 2671–2684.
[18] K. Sano, N. Oono, S. Ukai, S. Hayashi, T. Inoue, S. Yamashita, T. Yoshitake, γ″-Ni3Nb precipitate in Fe–Ni base alloy, J. Nucl. Mater. 442 (2013) 389–393.
[19] M. Burke, M. Miller, Precipitation in alloy 718: a combined Al3M and apfim investigation, in: E.A. Loria (Ed.), Superalloys 718, 625 and Various Derivatives, the Minerals, Metals & Materials Society, 1991.
[20] S. Azadian, L.-Y. Wei, R. Warren, Delta phase precipitation in Inconel 718, Mater. Char. 53 (2004) 7–16.
[21] S. Gribbin, S. Ghorbanpour, N.C. Ferreri, J. Bicknell, I. Tsukrov, M. Knezevic, Role of grain structure, grain boundaries, crystallographic texture, precipitates, and porosity on fatigue behavior of Inconel 718 at room and elevated temperatures, Mater. Char. 149 (2019) 184–197.
[22] E.A. Lass, M.R. Stoudt, M.E. Williams, M.B. Katz, L.E. Levine, T.Q. Phan, T. H. Gnaeupel-Herold, D.S. Ng, formation of the Ni3Nb δ-phase in stress-relieved inconel 625 produced via laser powder-bed fusion additive manufacturing, Metall. Mater. Trans. 48 (2017) 5547–5558.
[23] N.C. Ferreri, S.C. Vogel, M. Knezevic, Determining volume fractions of γ, γ′, γ″, δ, and MC-carbide phases in Inconel 718 as a function of its processing history using an advanced neutron diffraction procedure, Mater. Sci. Eng. 781 (2020) 139228.
[24] H. Gleiter, E. Hornbogen, Precipitation hardening by coherent particles, Mater. Sci. Eng. 2 (1968) 285–302.
[25] W. Huther, B. Reppich, Interaction of dislocations with coherent, stree-free ordered particles, Zeitschrift Fur Metallkunde 69 (1978) 628–634.
[26] K. Maciejewski, M. Jouiad, H. Ghonem, Dislocation/precipitate interactions in IN100 at 650°C, Mater. Sci. Eng. 582 (2013) 47–54.
[27] S. Ghorbanpour, M. Zecevic, A. Kumar, M. Jahedi, J. Bicknell, L. Jorgensen, I. J. Beyerlein, M. Knezevic, A crystal plasticity model incorporating the effects of precipitates in superalloys: application to tensile, compressive, and cyclic deformation of Inconel 718, Int. J. Plast. 99 (2017) 162–185.
[28] S. Ghorbanpour, M.E. Alam, N.C. Ferreri, A. Kumar, B.A. McWilliams, S.C. Vogel, J. Bicknell, I.J. Beyerlein, M. Knezevic, Experimental characterization and crystal plasticity modeling of anisotropy, tension-compression asymmetry, and texture evolution of additively manufactured Inconel 718 at room and elevated temperatures, Int. J. Plast. 125 (2020) 63–79.
[29] H. Haddou, M. Risbet, G. Marichal, X. Feaugas, The effects of grain size on the cyclic deformation behaviour of polycrystalline nickel, Mater. Sci. Eng. 379 (2004) 102–111.
[30] W. Österle, D. Bettge, B. Fedelich, H. Klingelhöffer, Modelling the orientation and direction dependence of the critical resolved shear stress of nickel-base superalloy single crystals, Acta Mater. 48 (2000) 689–700.
[31] Z. Ding, Y. Liu, Z. Yin, Z. Yang, X. Cheng, Study of elastoplastic constitutive model for single crystal nickel-based superalloy, Hangkong Dongli Xuebao/Journal of Aerospace Power 19 (2004) 755–761.
[32] S. Semiatin, P. Fagin, M. Glavicic, D. Raabe, Deformation behavior of Waspaloy at hot-working temperatures, Scripta Mater. 50 (2004) 625–629.
[33] S. Copley, B. Kear, Temperature and orientation dependence of the flow stress in off-stoichiometric Ni sub 3 Al/gamma' phase/(Strength characteristics of single crystals of nickel aluminide/gamma phase/, discussing temperature and orientation dependence of work hardening), AIME, TRANSACTIONS 239 (1967) 977–984.
[34] S. Copley, B. Kear, A dynamic theory of coherent precipitation hardening with application to nickel-base alloys(Coherent precipitation hardening theory treats yielding in nickel base alloy containing coherent stress-free ordered particles as dynamic process), AIME, TRANSACTIONS 239 (1967) 984–992.
[35] S. Keshavarz, S. Ghosh, A crystal plasticity finite element model for flow stress anomalies in Ni3Al single crystals, Phil. Mag. 95 (2015) 2639–2660.
[36] E. Schmid, W. Boas, Plasticity of Crystals with Special Reference to Metals, English translation F.A. Hughes, London, 1950.
[37] M. Dao, R.J. Asaro, Non-Schmid effects and localized plastic flow in intermetallic alloys, Mater. Sci. Eng. 170 (1993) 143–160.
[38] M. Knezevic, A. Bhattacharyya, Characterization of microstructure in Nb rods processed by rolling: effect of grooved rolling die geometry on texture uniformity, Int. J. Refract. Metals Hard Mater. 66 (2017) 44–51.
[39] A. Bhattacharyya, M. Knezevic, M. Abouaf, Characterization of crystallographic texture and intra-grain morphology in cross-rolled tantalum, Metall. Mater. Trans. 46 (2015) 1085–1096.
[40] J.-B. Baudouin, G. Monnet, M. Perez, C. Domain, A. Nomoto, Effect of the applied stress and the friction stress on the dislocation dissociation in face centered cubic metals, Mater. Lett. 97 (2013) 93–96.
[41] M. Shenoy, Y. Tjiptowidjojo, D. McDowell, Microstructure-sensitive modeling of polycrystalline IN 100, Int. J. Plast. 24 (2008) 1694–1730.
[42] L. Xiao, D.L. Chen, M.C. Chaturvedi, Shearing of γ″ precipitates and formation of planar slip bands in Inconel 718 during cyclic deformation, Scripta Mater. 52 (2005) 603–607.
[43] R.V. Miner, J. Gayda, R.D. Maier, Fatigue and creep-fatigue deformation of several nickel-base superalloys at 650 °c, Metallurgical Transactions A 13 (1982) 1755–1765.
[44] H.F. Merrick, The low cycle fatigue of three wrought nickel-base alloys, Metallurgical Transactions 5 (1974) 891–897.
[45] L. Xiao, D. Chen, M. Chaturvedi, Cyclic deformation mechanisms of precipitation-hardened Inconel 718 superalloy, Mater. Sci. Eng. 483 (2008) 369–372.
[46] D. Worthem, I. Robertson, F. Leckie, D. Socie, C. Altstetter, Inhomogeneous deformation in INCONEL 718 during monotonic and cyclic loadings, MTA 21 (1990) 3215–3220.
[47] M. Sundararaman, P. Mukhopadhyay, S. Banerjee, Deformation behaviour of γ ″strengthened Inconel 718, Acta Metall. 36 (1988) 847–864.
[48] S. Kalluri, K.B.S. Rao, G.R. Halford, M.A. McGaw, Deformation and damage mechanisms in Inonel 718 superalloy, in: Proc. Superalloys 718, 625, 706 and Various Derivatives the Minerals, Metals & Materials Society, 1994.
[49] D.W. Worthem, I.M. Robertson, F.A. Leckie, D.F. Socie, C.J. Altstetter, Inhomogeneous deformation in INCONEL 718 during monotonic and cyclic loadings, Metallurgical Transactions A 21 (1990) 3215–3220.
[50] J. He, S. Fukuyama, K. Yokogawa, Deformation bands in inconel 718, Mater. Sci. Technol. 11 (1995) 914–920.
[51] T.P. Gabb, G. Welsch, The high temperature deformation in cyclic loading of a single crystal nickel-base superalloy, Acta Metall. 37 (1989) 2507–2516.
[52] D. Fournier, A. Pineau, Low cycle fatigue behavior of Inconel 718 at 298 K and 823 K, MTA 8 (1977) 1095–1105.
[53] A. Banerjee, J. Sahu, N. Paulose, C. Fernando, R. Ghosh, Micromechanism of cyclic plastic deformation of alloy IN 718 at 600° C, Fatig. Fract. Eng. Mater. Struct. 39 (2016) 877–885.
[54] J. Eftis, M. Abdel-Kader, D. Jones, Comparisons between the modified Chaboche and Bodner-Partom viscoplastic constitutive theories at high temperature, Int. J. Plast. 5 (1989) 1–27.

[55] J. Chaboche, Modeling of the cyclic response and ratchetting effects on inconel-718 alloy, Eur. J. Mech. Solid. 10 (1991) 101–121.
[56] Z. Feng, S.-Y. Yoon, J.-H. Choi, T.J. Barrett, M. Zecevic, F. Barlat, M. Knezevic, A comparative study between elasto-plastic self-consistent crystal plasticity and anisotropic yield function with distortional hardening formulations for sheet metal forming, Mech. Mater. 148 (2020), 103422.
[57] A. Cruzado, J. Llorca, J. Segurado, Modeling cyclic deformation of inconel 718 superalloy by means of crystal plasticity and computational homogenization, Int. J. Solid Struct. 122–123 (2017) 148–161.
[58] C.P. Przybyla, D.L. McDowell, Microstructure-sensitive extreme value probabilities for high cycle fatigue of Ni-base superalloy IN100, Int. J. Plast. 26 (2010) 372–394.
[59] F.D. León-Cázares, F. Monni, T. Jackson, E.I. Galindo-Nava, C.M.F. Rae, Stress response and microstructural evolution of nickel-based superalloys during low cycle fatigue: physics-based modelling of cyclic hardening and softening, Int. J. Plast. 128 (2020), 102682.
[60] S. Berbenni, V. Favier, M. Berveiller, Impact of the grain size distribution on the yield stress of heterogeneous materials, Int. J. Plast. 23 (2007) 114–142.
[61] B. Raeisinia, C. Sinclair, W. Poole, C. Tomé, On the impact of grain size distribution on the plastic behaviour of polycrystalline metals, Model. Simulat. Mater. Sci. Eng. 16 (2008), 025001.
[62] R.A. Lebensohn, A.K. Kanjarla, P. Eisenlohr, An elasto-viscoplastic formulation based on fast Fourier transforms for the prediction of micromechanical fields in polycrystalline materials, Int. J. Plast. 32–33 (2012) 59–69.
[63] D.H. Smith, J. Bicknell, L. Jorgensen, B.M. Patterson, N.L. Cordes, I. Tsukrov, M. Knezevic, Microstructure and mechanical behavior of direct metal laser sintered Inconel alloy 718, Mater. Char. 113 (2016) 1–9.
[64] A. Eghtesad, M. Knezevic, High-performance full-field crystal plasticity with dislocation-based hardening and slip system back-stress laws: application to modeling deformation of dual-phase steels, J. Mech. Phys. Solid. 134 (2020), 103750.
[65] A.J. Beaudoin, P.R. Dawson, K.K. Mathur, U.F. Kocks, D.A. Korzekwa, Application of polycrystal plasticity to sheet forming. Comput. Methods Appl. Mech. Eng. 117 (1994) 49–70.
[66] M. Ardeljan, I.J. Beyerlein, M. Knezevic, A dislocation density based crystal plasticity finite element model: application to a two-phase polycrystalline HCP/BCC composites, J. Mech. Phys. Solid. 66 (2014) 16–31.
[67] M. Knezevic, B. Drach, M. Ardeljan, I.J. Beyerlein, Three dimensional predictions of grain scale plasticity and grain boundaries using crystal plasticity finite element models, Comput. Methods Appl. Mech. Eng. 277 (2014) 239–259.
[68] M. Ardeljan, M. Knezevic, Explicit modeling of double twinning in AZ31 using crystal plasticity finite elements for predicting the mechanical fields for twin variant selection and fracture analyses, Acta Mater. 157 (2018) 339–354.
[69] M. Ardeljan, M. Knezevic, T. Nizolek, I.J. Beyerlein, N.A. Mara, T.M. Pollock, A study of microstructure-driven strain localizations in two-phase polycrystalline HCP/BCC composites using a multi-scale model, Int. J. Plast. 74 (2015) 35–57.
[70] S.R. Kalidindi, H.K. Duvvuru, M. Knezevic, Spectral calibration of crystal plasticity models, Acta Mater. 54 (2006) 1795–1804.
[71] M. Ardeljan, R.J. McCabe, I.J. Beyerlein, M. Knezevic, Explicit incorporation of deformation twins into crystal plasticity finite element models, Comput. Methods Appl. Mech. Eng. 295 (2015) 396–413.
[72] M. Ardeljan, D.J. Savage, A. Kumar, I.J. Beyerlein, M. Knezevic, The plasticity of highly oriented nano-layered Zr/Nb composites, Acta Mater. 115 (2016) 189–203.
[73] A. Eghtesad, M. Zecevic, R.A. Lebensohn, R.J. McCabe, M. Knezevic, Spectral database constitutive representation within a spectral micromechanical solver for computationally efficient polycrystal plasticity modelling, Comput. Mech. 61 (2018) 89–104.
[74] A. Eghtesad, T.J. Barrett, K. Germaschewski, R.A. Lebensohn, R.J. McCabe, M. Knezevic, OpenMP and MPI implementations of an elasto-viscoplastic fast Fourier transform-based micromechanical solver for fast crystal plasticity modeling, Adv. Eng. Software 126 (2018) 46–60.
[75] R.A. Lebensohn, N-site modeling of a 3D viscoplastic polycrystal using fast Fourier transform, Acta Mater. 49 (2001) 2723–2737.
[76] J.W. Hutchinson, Bounds and self-consistent estimates for creep of polycrystalline materials, Proc. Roy. Soc. Lond. Math. Phys. Sci. 348 (1976) 101–126.
[77] R.J. Asaro, A. Needleman, Texture development and strain hardening in rate dependent polycrystals, Acta Metall. Mater. 33 (1985) 923–953.
[78] M. Knezevic, M. Zecevic, I.J. Beyerlein, R.A. Lebensohn, A numerical procedure enabling accurate descriptions of strain rate-sensitive flow of polycrystals within crystal visco-plasticity theory, Comput. Methods Appl. Mech. Eng. 308 (2016) 468–482.
[79] M. Zecevic, I.J. Beyerlein, R.J. McCabe, B.A. McWilliams, M. Knezevic, Transitioning rate sensitivities across multiple length scales: microstructure-property relationships in the Taylor cylinder impact test on zirconium, Int. J. Plast. 84 (2016) 138–159.
[80] D.J. Savage, I.J. Beyerlein, M. Knezevic, Coupled texture and non-Schmid effects on yield surfaces of body-centered cubic polycrystals predicted by a crystal plasticity finite element approach, Int. J. Solid Struct. 109 (2017) 22–32.
[81] M. Zecevic, M. Knezevic, A new visco-plastic self-consistent formulation implicit in dislocation-based hardening within implicit finite elements: application to high strain rate and impact deformation of tantalum, Comput. Methods Appl. Mech. Eng. 341 (2018) 888–916.
[82] M. Knezevic, S.R. Kalidindi, Fast computation of first-order elastic-plastic closures for polycrystalline cubic-orthorhombic microstructures, Comput. Mater. Sci. 39 (2007) 643–648.
[83] N. Landry, M. Knezevic, Delineation of first-order elastic property closures for hexagonal metals using fast fourier transforms, Materials 8 (2015) 6326–6345.
[84] X. Wu, G. Proust, M. Knezevic, S.R. Kalidindi, Elastic-plastic property closures for hexagonal close-packed polycrystalline metals using first-order bounding theories, Acta Mater. 55 (2007) 2729–2737.
[85] S.R. Kalidindi, M. Knezevic, S. Niezgoda, J. Shaffer, Representation of the orientation distribution function and computation of first-order elastic properties closures using discrete Fourier transforms, Acta Mater. 57 (2009) 3916–3923.
[86] T. Fast, M. Knezevic, S.R. Kalidindi, Application of microstructure sensitive design to structural components produced from hexagonal polycrystalline metals, Comput. Mater. Sci. 43 (2008) 374–383.
[87] R. Bellman, G. Adomian, Green's functions for partial differential equations, in: Partial Differential Equations, Springer, 1985, pp. 243–247.
[88] A.I. Zayed, A convolution and product theorem for the fractional Fourier transform, IEEE Signal Process. Lett. 5 (1998) 101–103.
[89] J. Michel, H. Moulinec, P. Suquet, A computational scheme for linear and non-linear composites with arbitrary phase contrast, Int. J. Numer. Methods Eng. 52 (2001) 139–160.
[90] H. Moulinec, F. Silva, Comparison of three accelerated FFT-based schemes for computing the mechanical response of composite materials, Int. J. Numer. Methods Eng. 97 (2014) 960–985.
[91] J. Michel, H. Moulinec, P. Suquet, A computational method based on augmented Lagrangians and fast Fourier transforms for composites with high contrast, CM 1 (2000) 79–88.
[92] T.H. Courtney, Mechanical Behavior of Materials, Waveland Press, 2005.
[93] K. Kitayama, C. Tomé, E. Rauch, J. Gracio, F. Barlat, A crystallographic dislocation model for describing hardening of polycrystals during strain path changes, Application to low carbon steels 46 (2013) 54–69.
[94] M. Zecevic, Y.P. Korkolis, T. Kuwabara, M. Knezevic, Dual-phase steel sheets under cyclic tension–compression to large strains: experiments and crystal plasticity modeling, J. Mech. Phys. Solid. 96 (2016) 65–87.
[95] M. Zecevic, M. Knezevic, Latent hardening within the elasto-plastic self-consistent polycrystal homogenization to enable the prediction of anisotropy of AA6022-T4 sheets, Int. J. Plast. 105 (2018) 141–163.
[96] F.F. Lavrentev, The type of dislocation interaction as the factor determining work hardening, Mater. Sci. Eng. 46 (1980) 191–208.
[97] H. Mecking, U.F. Kocks, Kinetics of flow and strain-hardening, Acta Metall. Mater. 29 (1981) 1865–1875.
[98] M. Knezevic, I.J. Beyerlein, M.L. Lovato, C.N. Tomé, A.W. Richards, R.J. McCabe, A strain-rate and temperature dependent constitutive model for BCC metals incorporating non-Schmid effects: application to tantalum–tungsten alloys, Int. J. Plast. 62 (2014) 93–104.
[99] M. Knezevic, M. Zecevic, I.J. Beyerlein, J.F. Bingert, R.J. McCabe, Strain rate and temperature effects on the selection of primary and secondary slip and twinning systems in HCP Zr, Acta Mater. 88 (2015) 55–73.
[100] M. Knezevic, R.J. McCabe, C.N. Tomé, R.A. Lebensohn, S.R. Chen, C.M. Cady, G. T. Gray Iii, B. Mihaila, Modeling mechanical response and texture evolution of α-uranium as a function of strain rate and temperature using polycrystal plasticity, Int. J. Plast. 43 (2013) 70–84.
[101] U.F. Kocks, H. Mecking, Kinetics of flow and strain-hardening, Acta Metall. 29 (1981) 1865–1875.
[102] U.F. Kocks, H. Mecking, Physics and phenomenology of strain hardening: the FCC case, Prog. Mater. Sci. 48 (2003) 171–273.
[103] K. Kitayama, C. Tomé, E. Rauch, J. Gracio, F. Barlat, A crystallographic dislocation model for describing hardening of polycrystals during strain path changes. Application to low carbon steels, Int. J. Plast. 46 (2013) 54–69.
[104] M. Zecevic, M. Knezevic, An implicit formulation of the elasto-plastic self-consistent polycrystal plasticity model and its implementation in implicit finite elements, Mech. Mater. 136 (2019), 103065.
[105] I.J. Beyerlein, C.N. Tomé, A dislocation-based constitutive law for pure Zr including temperature effects, Int. J. Plast. 24 (2008) 867–895.
[106] W. Wen, M. Borodachenkova, C. Tomé, G. Vincze, E. Rauch, F. Barlat, J.J. Grácio, Mechanical behavior of Mg subjected to strain path changes, experiments and modeling 73 (2015) 171–183.
[107] R. Madec, B. Devincre, L. Kubin, T. Hoc, D.J.S. Rodney, The role of collinear interaction in dislocation-induced hardening 301 (2003) 1879–1882.
[108] P.J. Jackson, Dislocation modelling of shear in f.c.c. crystals, Prog. Mater. Sci. 29 (1985) 139–175.
[109] Z. Wang, I. Beyerlein, R. LeSar, The importance of cross-slip in high-rate deformation, Model. Simulat. Mater. Sci. Eng. 15 (2007) 675.
[110] B. Peeters, B. Bacroix, C. Teodosiu, P. Van Houtte, E. Aernoudt, Work-hardening/softening behaviour of b.c.c. polycrystals during changing strain paths: II. TEM observations of dislocation sheets in an IF steel during two-stage strain paths and their representation in terms of dislocation densities, Acta Mater. 49 (2001) 1621–1632.
[111] M. Zecevic, M. Knezevic, I.J. Beyerlein, R.J. McCabe, Texture formation in orthorhombic alpha-uranium under simple compression and rolling to high strains, J. Nucl. Mater. 473 (2016) 143–156.
[112] M. Zecevic, M. Knezevic, I.J. Beyerlein, R.J. McCabe, Origin of texture development in orthorhombic uranium, Mater. Sci. Eng. 665 (2016) 108–124.
[113] A.M. Cantara, M. Zecevic, A. Eghtesad, C.M. Poulin, M. Knezevic, Predicting elastic anisotropy of dual-phase steels based on crystal mechanics and microstructure, Int. J. Mech. Sci. 151 (2019) 639–649.
[114] E.V. Nesterova, S. Bouvier, B. Bacroix, Microstructure evolution and mechanical behavior of a high strength dual-phase steel under monotonic loading, Mater. Char. 100 (2015) 152–162.

[115] L.P. Evers, W.A.M. Brekelmans, M.G.D. Geers, Non-local crystal plasticity model with intrinsic SSD and GND effects, J. Mech. Phys. Solid. 52 (2004) 2379–2401.
[116] R.A. Lebensohn, A. Needleman, Numerical implementation of non-local polycrystal plasticity using fast Fourier transforms, J. Mech. Phys. Solid. 97 (2016) 333–351.
[117] K.S. Djaka, S. Berbenni, V. Taupin, R.A. Lebensohn, A FFT-based numerical implementation of mesoscale field dislocation mechanics: application to two-phase laminates, Int. J. Solid Struct. 184 (2020) 136–152.
[118] S. Berbenni, V. Taupin, R.A. Lebensohn, A fast Fourier transform-based mesoscale field dislocation mechanics study of grain size effects and reversible plasticity in polycrystals, J. Mech. Phys. Solid. 135 (2020), 103808.
[119] M.D. Uchic, M.A. Groeber, D.M. Dimiduk, J.P. Simmons, 3D microstructural characterization of nickel superalloys via serial-sectioning using a dual beam FIB-SEM, Scripta Mater. 55 (2006) 23–28.
[120] A. Adelmann, R.D. Ryne, J. Shalf, C. Siegerist, H5part: a portable high performance parallel data interface for particle simulations, in: Proceedings of the 2005 Particle Accelerator Conference, IEEE, 2005, pp. 4129–4131.
[121] U. Ayachit, The Paraview Guide: a Parallel Visualization Application, 2015.
[122] M. Kabel, D. Merkert, M. Schneider, Use of composite voxels in FFT-based homogenization, Comput. Methods Appl. Mech. Eng. 294 (2015) 168–188.
[123] P. Haldipur, Material Characterization of Nickel-Based Super Alloys through Ultrasonic Inspection, Iowa State University, Ames, Iowa, 2006.
[124] B. Devincre, L. Kubin, T. Hoc, Physical analyses of crystal plasticity by DD simulations, Scripta Mater. 54 (2006) 741–746.
[125] EOS NickelAlloy IN718 Data Sheet, EOS GmbH - Electro Optical Systems, 2014. http://www.eos.info/material-m.
[126] J. Stinville, W. Lenthe, J. Miao, T. Pollock, A combined grain scale elastic–plastic criterion for identification of fatigue crack initiation sites in a twin containing polycrystalline nickel-base superalloy, Acta Mater. 103 (2016) 461–473.
[127] J.-C. Stinville, W.C. Lenthe, M.P. Echlin, P.G. Callahan, D. Texier, T.M. Pollock, Microstructural statistics for fatigue crack initiation in polycrystalline nickel-base superalloys, Int. J. Fract. 208 (2017) 221–240.
[128] J. Stinville, N. Vanderesse, F. Bridier, P. Bocher, T. Pollock, High resolution mapping of strain localization near twin boundaries in a nickel-based superalloy, Acta Mater. 98 (2015) 29–42.
[129] J.C. Stinville, E. Martin, M. Karadge, S. Ismonov, M. Soare, T. Hanlon, S. Sundaram, M.P. Echlin, P.G. Callahan, W.C. Lenthe, Fatigue deformation in a polycrystalline nickel base superalloy at intermediate and high temperature: competing failure modes, Acta Mater. 152 (2018) 16–33.
[130] A. Eghtesad, M. Knezevic, A new approach to fluid–structure interaction within graphics hardware accelerated smooth particle hydrodynamics considering heterogeneous particle size distribution, Computational Particle Mechanics 5 (2018) 387–409.
[131] A. Eghtesad, K. Germaschewski, I.J. Beyerlein, A. Hunter, M. Knezevic, Graphics processing unit accelerated phase field dislocation dynamics: application to bi-metallic interfaces, Adv. Eng. Software 115 (2018) 248–267.